AGU ADVANCING EARTH AND SPACE SCIENCE

Geophysical Research Letters

RESEARCH LETTER
10.1029/2021GL093723

Key Points:

- The full process of a landslide hazard chain on February 7, 2021 in the Himalayas is reconstructed using cell-based numerical simulation
- The analysis explicitly explains the volume amplification and hazard type transformation in the hazard chain
- The erosion and deposition features during the hazard chain process are also quantified

Supporting Information:

Supporting Information may be found in the online version of this article.

Correspondence to:

L. Zhang,
cezhangl@ust.hk

Citation:

Jiang, R., Zhang, L., Peng, D., He, X., & He, J. (2021). The landslide hazard chain in the Tapovan of the Himalayas on 7 February 2021. *Geophysical Research Letters*, *48*, e2021GL093723. https://doi.org/10.1029/2021GL093723

Received 5 APR 2021
Accepted 13 AUG 2021

The Landslide Hazard Chain in the Tapovan of the Himalayas on 7 February 2021

Ruochen Jiang[1], Limin Zhang[1,2], Dalei Peng[1], Xin He[1], and Jian He[1]

[1]Department of Civil and Environmental Engineering, The Hong Kong University of Science and Technology, Hong Kong, China, [2]Shenzhen Research Institute, The Hong Kong University of Science and Technology, Shenzhen, China

Abstract On February 7, 2021, a catastrophic landslide occurred in Chamoli, India on the southern hills of the Himalayas (30.37°N, 79.73°E). About 28×10^6 m^3 of landslide mass detached from the mountain face, entrained deposits in the valley and riverbed, and generated a huge debris flood along the Dhauliganga River. In this study, the geomorphological and volumetric characteristics of the disaster chain were interpreted from satellite images. The full process of the disaster chain and the erosion, deposition and flow discharge processes were reproduced using a cell-based analysis program, Erosion–Deposition Debris Flow Analysis (EDDA). The results indicate a peak flow discharge of the debris flood at Tapovan Hydropower Station of about 25,000–28,000 m^3/s. The main erosion and deposition zones are distributed along the valley floor and the Dhauliganga River, respectively. This study serves as basis for understanding the disaster chain dynamics in high mountain areas.

Plain Language Summary Catastrophic geo-disasters become more frequent in the Himalayan region due to the global climate change, and pose threats to the local residents and infrastructure. A large landslide happened in the Tapovan area in the south of the Himalayas on February 7, 2021, which triggered a large avalanche down the valley, entrained the deposits and river water, and evolved into a catastrophic debris flood in the Dhauliganga River, causing fatalities and severe damage to the local infrastructure. This study reconstructs the entire geo-disaster process, and reveals key characteristics including the landslide source, erosion and deposition features, and the transformation of hazard types. The outcome from this study helps understand and manage the risk of catastrophic geo-hazards in high mountain areas, especially in the Himalayas and other areas of the Tibetan Plateau.

1. Introduction

As an "amplifier" of global climate change, the Himalayan belt with extensive glacierized extent is sensitive to the changing climatic conditions (Farinotti, Huss, & Fürst, 2019; Farinotti, Round, & Huss, 2019; Immerzeel et al., 2010; Scherler et al., 2011). Widespread recession of glaciers is occurring on the plateau as a result of climate change and anthropogenic forcing (IPCC, 2013, 2019; Marzeion et al., 2014; Wang et al., 2021; Zemp et al., 2019). As glaciers melt, accelerated water infiltration into the superficial geomaterials (Grämiger et al., 2020) and permafrost thaw (Gruber et al., 2004) take place, resulting in reduced strengths of the geo-materials and hence landslides at high altitudes. At about 10:00 a.m. local time (04:30 GMT) on February 7, 2021 (Martha et al., 2021), an enormous landslide occurred near Nanda Ghunti (30.37°N, 79.73°E) in India's Chamoli District (Figure 1a). The massive ice and soil avalanche rushed into a valley and eventually triggered a large debris flood, causing serious damage to local hydropower stations and bridges along the Dhauliganga River. The flood caused more than 200 fatalities or missing individuals (Shugar et al., 2021). It was one of the most catastrophic geo-disasters on record in this region, and attracted wide attentions (Martha et al., 2021; Meena et al., 2021; Pandey et al., 2021; Rana et al., 2021; Shrestha et al., 2021).

Before this landslide, an unstable wedge block and tension cracks were visible on the north flank of the landslide scar on February 6, 2021 (Figure S5). On February 7, 2021, the landslide source mass detached from the top of the glaciated steep mountain ridge at an elevation of 5,550 m (Figure 1b), and plunged into the valley at an elevation of approximately 3,800 m. After arriving the valley floor, the sliding block had fragmented and formed a huge avalanche moving down the valley channel. The debris traveled 13.9 km, with a large height relief from elevation 3,800–1,900 m, and entered the Dhauliganga River. On the way,

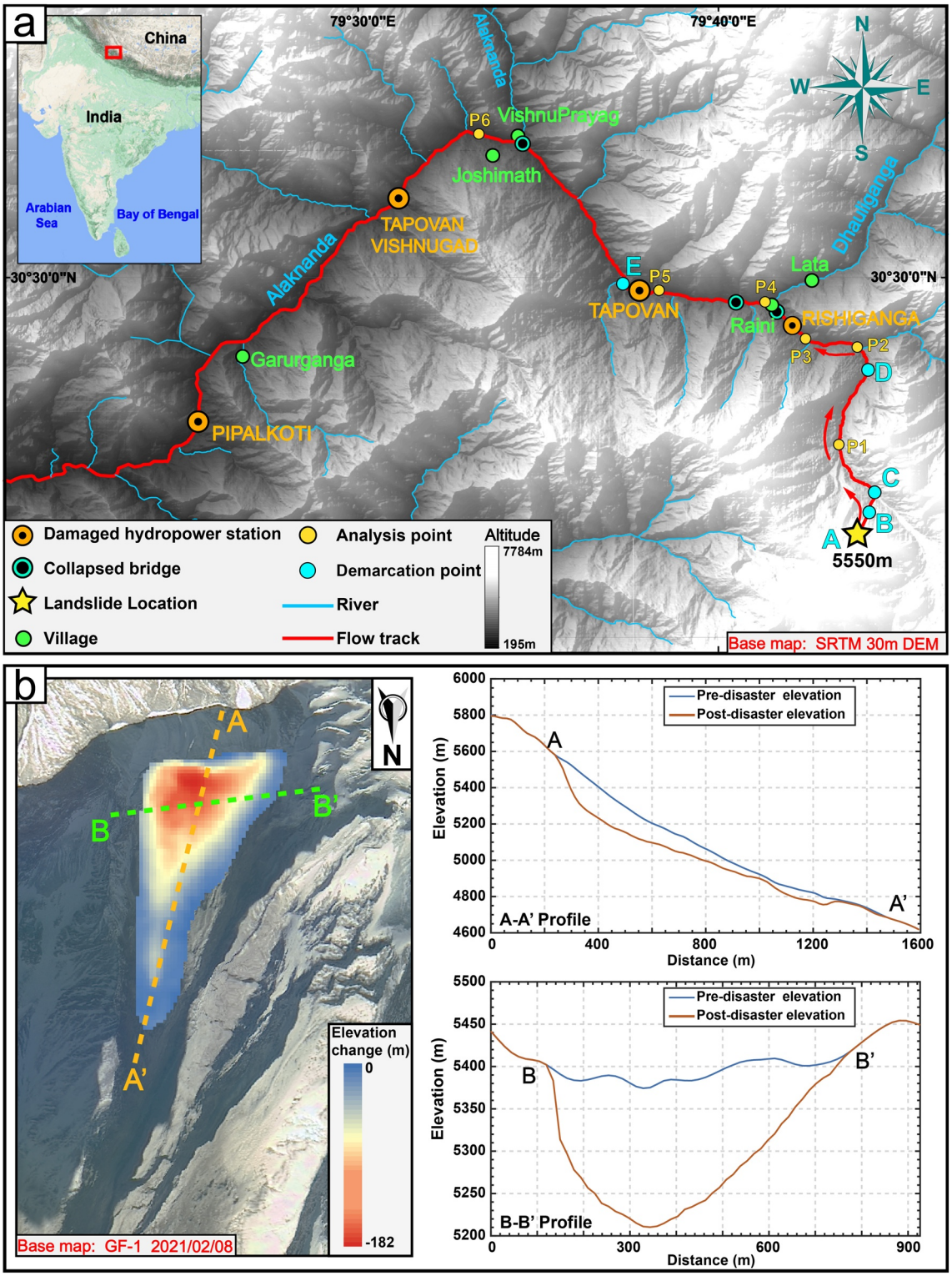

Figure 1. Landslide location and geomorphic features. (a) Regional map indicating the landslide location and affected areas. (b) Pre-sliding (October 25, 2020) and post-sliding (February 20, 2021) profile of landslide area (elevation derived from ZY-3 stereo data).

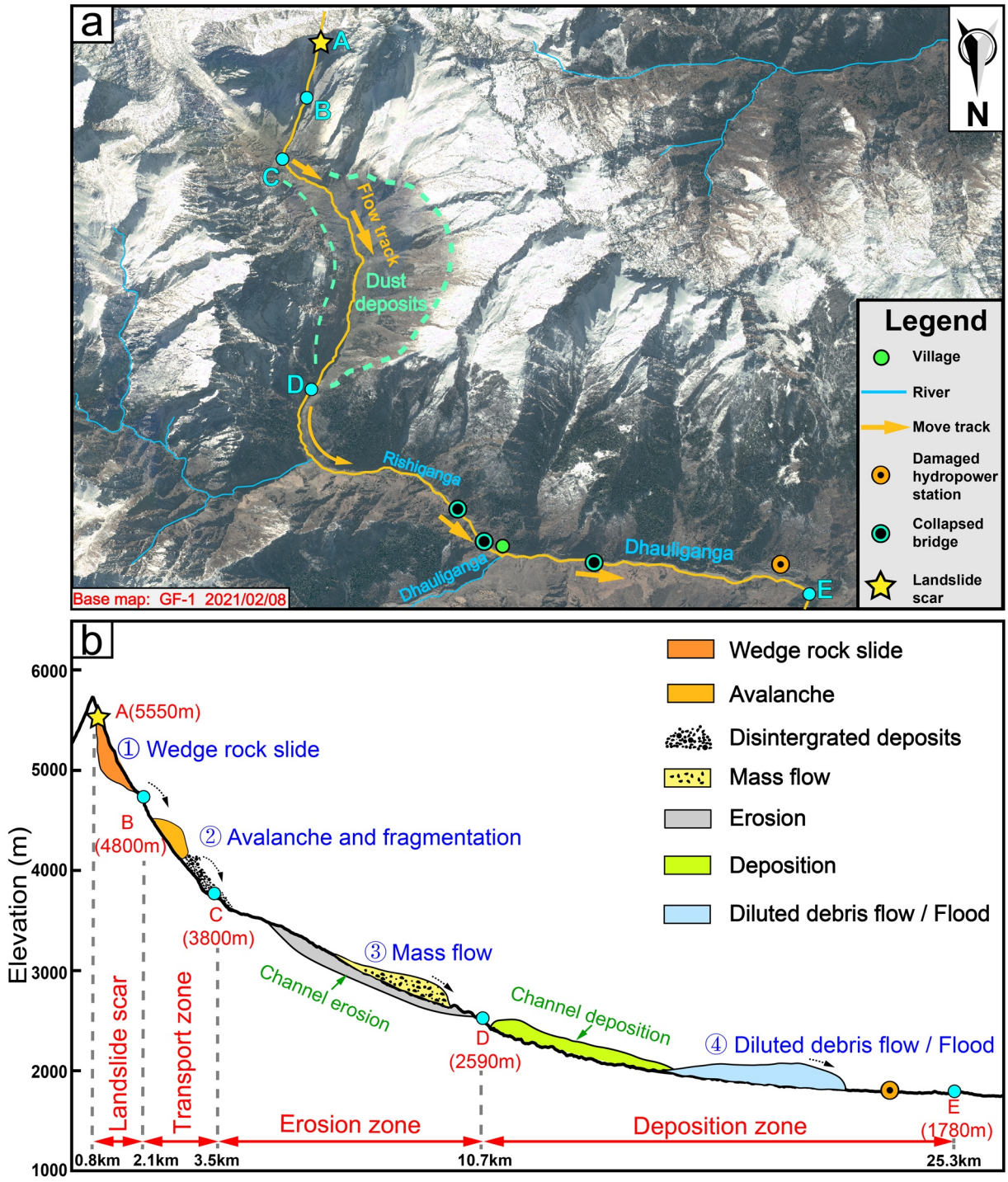

Figure 2. (a) Three-dimensional diagram of the hazard chain; (b) Hazard type transformation in different movement stages.

the mass flow generated and mobilized a vast quantity of dust, which finally deposited on the flanks of the valley (Figure 2a).

Previous research (Harris et al., 2014; Kumar et al., 2020; Mitchell & Jones, 2005) indicates that there has been a clear warming trend over the past decade in this region. Kumar et al. (2020) reported that the glacier extent in this valley decreased by 10% between 1980 and 2017, which may be the cause of the occurrence of geo-hazards in this area in the past few decades, such as the 2016 ice avalanche (Watson, 2021). The

event on February 7, 2021 happened after the warmest January in the last six decades in Uttarakhand and a post-monsoon season featuring high snowlines on the adjacent glaciers (Pelto, 2021). The meteorological data (Figure S6) shows that there was an obvious temperature rise from February 5 to February 7, 2021 during which heavy snowfall occurred. The increasing trend of geo-disasters emerges as a major issue in the high mountain region covered by glaciers, potentially causing more cascading hazards on the downstream settlements (Kirschbaum et al., 2020). These catastrophic geo-disasters and corresponding chain disasters also impose high risks on the construction and operation of hydropower projects in high mountains (Farinotti, Round, & Huss, 2019), particularly in the Himalayan and other Tibetan areas where various engineering projects are being constructed. Understanding the whole disaster chain process is vital to the management of geo-hazards in the region.

This study aims to reconstruct the disaster chain process that occurred in India's Chamoli District. The processes of the avalanche in the valley, changes of hazard types, and the propagation of the debris flood along the Dhauliganga River are simulated, and results of kinematic features, flow velocity and deposits are presented.

2. Data Sources

Table S1 summarizes all data for this study. Multi-source remote images were used to investigate the propagation of the tension cracks at the crown of the scar before the landslide occurred. Optical images from GF-1 (2.0 m resolution), GF-6 (2.0 m resolution), GF-7 (0.65 m resolution), Pléiades (0.5 m resolution), ZY-3 (2.5 m resolution), and Sentinel-2 (10 m resolution) were used to delineate the geometric features including the boundaries of the sliding wedge block (Figure S5), and the entrainment and deposition features along the flow path (Figure S7). Moreover, the meteorological data (Figure S6) before and after the landslide, including temperature, hourly precipitation and snowfall, has been collected from Meteoblue (Meteoblue Weather Maps, 2021) at 30.39°N 79.72°E.

The basic geographic information, including the terrain and local river system, was acquired (Table S1) and processed in ArcGIS. SRTM DEM was taken as the base terrain map to reflect the regional elevation features (Figure 1a), and the data from OpenSteetMap was used to reflect river distribution. The ground surface elevation changes before and after the disaster were calculated based on the ZY-3 stereo data (2.5 m resolution) on October 25, 2020 and February 20, 2021. The DEM production process and uncertainty estimation are presented in Text S3.

3. Geomorphological Characteristics

According to the local geological features and the interpretation of remote sensing, the geo-disaster chain can be divided into four zones as shown in Figure 2: the landslide scar (A-B), the transport zone (B-C), the entrainment zone (C-D), and the deposition and debris flood zone (D-E). Transformation of geo-disaster types is involved in these stages. In addition, the downstream areas of the Tapovan hydropower station on the Dhauliganga River were also affected by the generated debris flood.

As shown in Figure 2, the unstable wedge block is located at the top of a steep glaciated slope 35° – 45° in inclination angle, where the crest and toe elevations are 5,550 m and 4,800 m, respectively. Nearly East-West trending tension cracks formed on the crown before January 16, 2021 (Figures S5a–S5d), and the lateral boundary of the sliding wedge block covered with heavy snow can be delineated in the satellite image acquired by GF-6 (Figure S5h). Furthermore, Figures S6d and S6e indicate heavy snowfall in this region prior to the landslide (Figure S6). The landslide occurred during the period of rising temperature (Figure S6a). The source area covers almost 0.5 km^2 on the steep glaciated slope, more than 1,200 m along the slope direction and 550 m transversally along the crest. By analyzing the DEMs acquired by ZY-3 before and after the landslide, the volume of the detached landslide mass (i.e., rock mixed with ice and snow) was calculated to be 28 ± 0.62 million m^3, which is close to the estimated volume of 26.9 million m^3 in Shugar et al. (2021) and 29.3 million m^3 in Martha et al. (2021). The maximum vertical and normal thicknesses of the landslide mass are 182 ± 1.23 m and 130 ± 0.88 m, respectively (Figure 1b).

Between elevations 4,800 m and 3,800 m, the sliding mass advanced in the form of an avalanche, and formed disintegrated deposits at the valley floor. The avalanche impacted into the valley floor at about elevation 3,800 m, turning into a mass flow along the valley channel, spanning from elevation 3,800–2,590 m and covering a distance of 7.2 km (Figure 2). The satellite image shows riverbed materials in segment C-D before the landslide (Figure S8b). The high kinetic energy of the mass flow mobilized part of the glacial till and other deposits in the valley bed, and entrained them downwards into the Dhauliganga River. The differences of the erosion zones before and after the landslide are shown in Figure S7. The erosion process formed a V-shape channel in the valley floor (Figures S8b and S8c), and caused the mass flow volume to increase. The avalanche and mass flow also generated dust that deposited on both sides of the valley (Figure 2a), which was confirmed by Meena et al. (2021) using spectral reflectance from PlanetScope satellite imagery.

Segment D-E in Figure 2 and its downstream area were the main deposition area of the landslide mass. The mass flow destroyed the bridges over the Rishiganga River, and brought a large amount of debris into the Dhauliganga River, even causing the deposition in the upstream area near the intersection between the Rishiganga River and the Dhauliganga River (Figure S7g). The mass flow with high kinetic energy triggered a diluted debris flow along the river channel, and mobilized the debris and deposits from the erosion area, covering both sides of the river. The flood even affected Srinagar 150 km downstream (Emergency Response Coordination Centre [ERCC], 2021). A large amount of deposits had silted up the river, and caused structural damage to the Tapovan dam. The lower part of the dam was totally covered by debris. After deposition, the widths of the upstream and downstream channels of the Tapovan dam increased to about 80 and 40 m, respectively (Figure S8).

4. Simulation of the Geo-Hazard Chain

The integrated model EDDA (Erosion–Deposition Debris Flow Analysis), developed by Chen and Zhang (2015), Shen et al. (2020), and Zhou et al. (2019) was employed in this study to reproduce the geo-hazard chain process. In EDDA, the volumetric sediment concentration of the flow mixture, C_V, is employed to indicate the flow types of the mixture in a chain process. More details about EDDA are available at Supporting Information S1, and the model parameters used in the EDDA model are summarized in Text S2, Tables S2 and S3. The main features of the hazard chain are quantified based on the simulation results to reveal the erosion and deposition areas, the hazard types and flow discharge in the process.

Figure 3 shows the velocity of the mass flow along the channel at different snapshots. The mass movement reaches a high velocity (about 65 m/s) due to the steep terrain (Figures 3a and 3b). Such a rapid mass movement has also been observed in other recent large landslide disasters (Allstadt, 2013; Zhang et al., 2019). After flowing into the Rishganga River valley, the velocity of the mass flow decreases, and maintains at about 20 m/s until the flow enters the Dhauliganga River (Figure 3c). This stage is a typical process of debris flow movement in glacial areas of high altitudes like the Sedongpu debris flow in the Yarlung Tsangpo Grand Canyon (Wang et al., 2020). Subsequently, the mass flow travels downstream and flows through the Tapovan hydropower station at a velocity of about 12 m/s (Figure 3e). Compared with the post-event satellite image, the simulated inundation area is consistent with the actual flow boundaries shown in Figure 3e.

The volumetric sediment concentration of the mixture, C_V, is taken as a physical quantity to analyze types of the mass flow at different locations (Figure 4b). Moreover, a longitudinal section along the motion direction of the mass flow (the red line in Figure 4a) and six cross sections (the cyan points in Figure 4a) are picked to present simulation results. The color contours (Figure 4b) show three different areas divided by the green and blue dashed line, which indicate the different types of mass flow in different locations and times. The soild ratio in the mass flow witnesses an obvious decline with the increasing flow distance, which is also revealed in Shugar et al. (2021). It is obvious that the C_V values in the area below the dashed blue line in Figure 4b are kept at about 0.4 at all times, which indicates that the moving mass flow in this section has a relatively higher solid content. The solid materials mainly consist of the disintegrated landslide deposits and the entrained channel debris. Between the green and blue lines in Figure 4b, C_V features the material composition of the mass flow in section D-E (Figure 4a). In this section, the relatively high C_V value (0.4–0.5) indicates that the mass flow has relatively high solid contents in the first few minutes. However, the mass flow gradually transforms into a debris flood, which is reflected by smaller C_V values (<0.15). Based on the

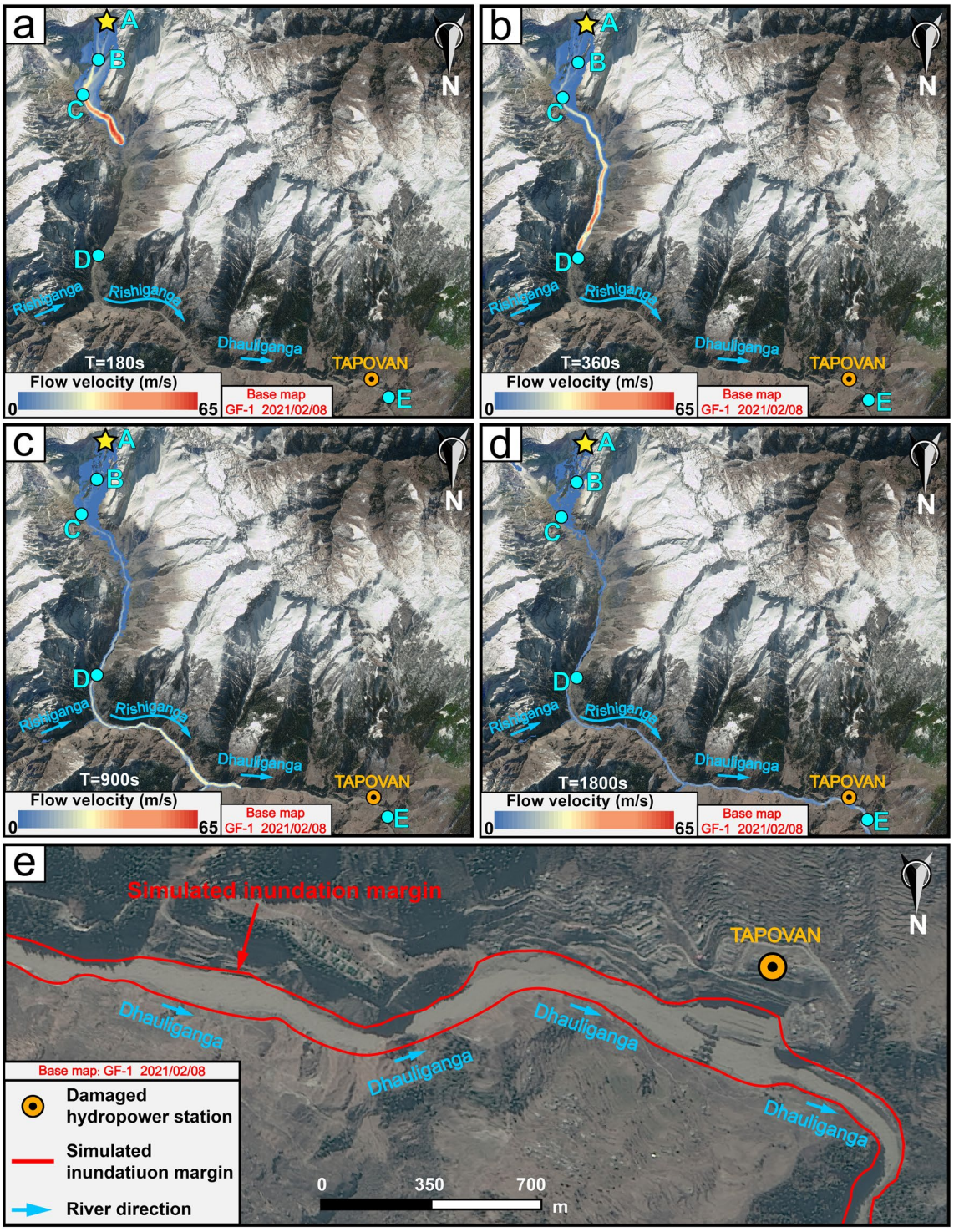

Figure 3. Simulated flow process along the channel. (a) T = 180 s. (b) T = 360 s. (c) T = 900 s. (d) T = 1,800 s. (e) Simulated inundation area near the Tapovan hydropower station.

regional hydrological information, it is the entrainment of the saturated bed materials and river water by the fast-moving mass flow that resulted in increased water contents of the moving mixture. After flowing through point E, the diluted debris flow turned into a large debris flood and rushed downstream as shown in the area above the green dashed line in Figure 4b.

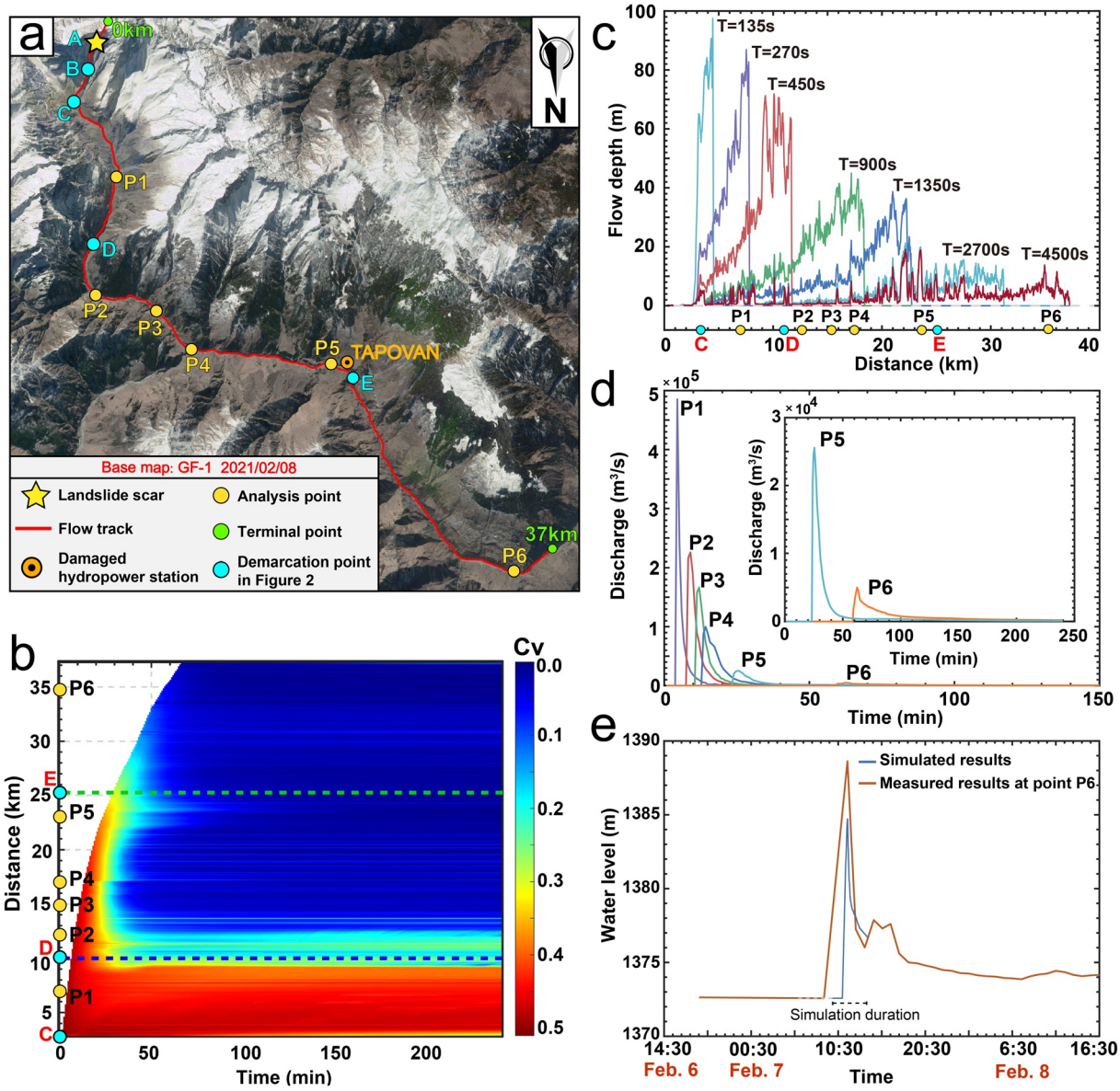

Figure 4. Transformation of hazard types revealed by the simulation results, and flow depths and discharges along the channel. (a) Selected longitudinal and cross sections. (b) C_V values along the selected longitudinal section at different times. (c) Flow depths at different times. (d) Discharges at different times. (e) Water level at point P6.

Figure 4c shows the flow depths at different times, and Text S5 presents the validation of the simulated results. The flow depth is more than 80 m in the early stages, and is maintained at large values. With the increase of the traveling distance, the flow depth decreases with the dispersion of the debris in space and the deposition of part of the debris. Based on the obtained flow depths and flow velocities, the discharge rates at the selected cross sections are calculated (Figure 4d). The disintegrated landslide deposits and the entrained materials contribute to the large discharge at point P1, which reveals the typical discharge features in the erosion areas. The discharge of the diluted debris flow in the deposition area can be directly reflected by curves P2, P3, and P4 in Figure 4d; the discharge decreases along the flow path. Curve P5 shows the discharge of the debris flow into the hydropower stations. The debris flow with a peak discharge of approximately 25,000 m^3/s (flow discharge analysis in Text S4) brings a large amount of debris into the Tapovan hydropower station, causing channel silting. The obvious changes of C_V before and after flowing through the hydropower station (the dashed green line in Figure 4b) suggest the deposition of solid materials. The C_V

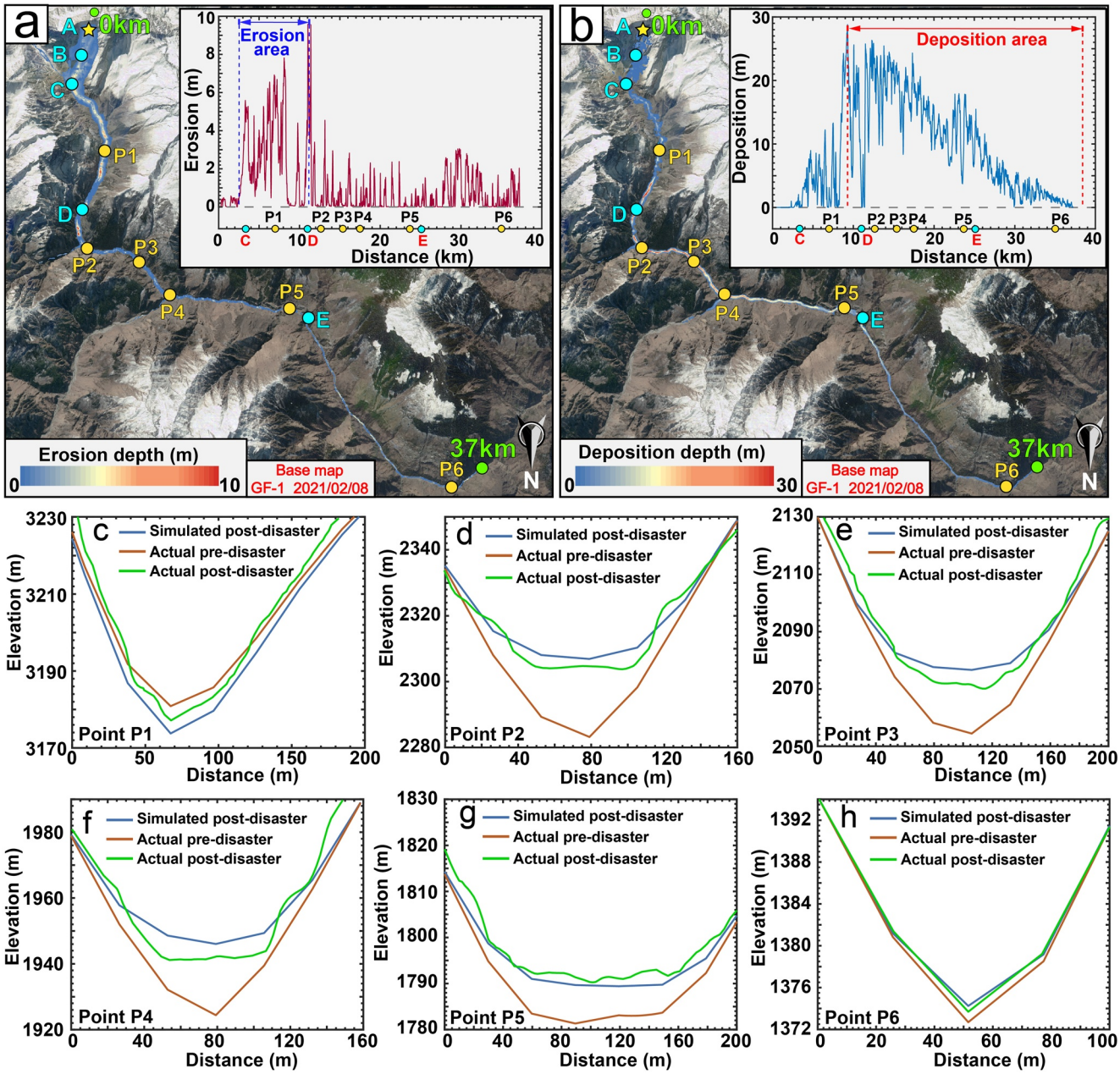

Figure 5. Erosion and deposition simulation results along the flow path and at the same analysis points in Figure 4. (a) Erosion simulation results along the channel. (b) Deposition simulation results along the channel. (c) Erosion at P1. (d) Deposition at P2. (e) Deposition at P3. (f) Deposition at P4. (g) Deposition at P5. (h) Deposition at P6.

value at point P6 (the Joshimath hydrometric station) further reveals that the debris flow has transformed into a debris flood (Figure 4b) with more than 10 m flow depth (Figure 4e). The results in Figure 4 verify the interpretation results in Figure 2 about the hazard types in different stages.

Figure 5 shows the final simulated erosion and deposition distributions along the longitudinal section (the red line in Figure 4a), and reveals simulated post-event elevations and actual pre- and post-event elevations (derived from ZY-3 for P1-P5; from on-site observation for P6) of the six cross sections at the same locations in Figure 4a. The thickness of deposits at point P6 is estimated based on the measured water level difference before and after the event (Figure 4e). The erosion process occurs primarily in segment C-D (Figure 5a) with erosion depths of 2–10 m, resulting in the formation of the V-shape channel in the valley floor (Figure 5c).

The rapidly moving mass flow entrained the existing saturated riverbed materials and river water in the valley bed, contributing to the volume amplification of the mass flow by 4.7 million m^3. It is worth noting that there is a small erosion area upstream of point P2 where the steep slope becomes relatively gentle and the moving direction of the mass flow sharply turns to the northwest. It can be found that deposition gradually dominates when the terrain becomes gentle (Figures 5a and 5b). After rushing into the Rishiganga River and the Dhauliganga River, the rapid mass flow gradually became a diluted debris flood along the river after the solid material gradually deposited. These have been correctly reflected by the calculated C_V values in Figure 4b. The thickness of the deposits gradually decreases in the downstream direction of the Dhauliganga River as shown in the Figures 5d–5h, which is consistent with the characteristics of elevation changes along the moving path in Shugar et al. (2021). A small amount of debris even deposits in the upstream area of the Dhauliganga River (Figure 5b). Affected by the deposition process, the downstream river channel turned into a U-shape (blue line in Figures 5d–5g).

5. Conclusions

This study investigates the recent catastrophic landslide hazard chain in the southern hill of the Himalayas in Chamoli, India. Remote sensing images were interpreted to analyze the disaster characteristics, and erosion and deposition numerical analysis was conducted to reconstruct the geo-hazard dynamic process. The analysis outcome serves as basis for understanding the geo-hazard chain dynamic process caused by landslides in high mountains covered with glacier. The main conclusions are summarized as follows:

1. The landslide source and its geometric features are interpreted from pre- and post-landslide satellite images. The landslide source is a sliding wedge block, 1,200 m in length, 182 m in maximum depth and 28 million m^3 in volume. Several cracks had formed around the landslide scar before the landslide.
2. The erosion and deposition areas are identified based on remote sensing techniques and numerical simulations. The erosion process mainly occurred in the valley between elevations 3,800 m and 2590 m, which contributes to much increased debris volume. The main deposition area is distributed along the Rishiganga River and the Dhauliganga River, and the deposition depth decreases along the flow path.
3. Transformation of geo-hazard types was involved in the different stages. The sliding wedge block detached from the steep slope and triggered a chain of hazards. The sliding rock blocks formed an avalanche down the valley, which entrained the saturated deposits in the valley floor. The changes in C_V along the flow path at different times reveal that the water content of the flowing mixture gradually increased after the mass flow rushed into the Rishiganga River and the Dhauliganga River, resulting in the formation of a huge diluted debris flood.

Data Availability Statement

The Gaofen-1 (GF-1), Gaofen-6 (GF-6), Gaofen-7 (GF-7), and Ziyuan-3 (ZY-3) satellite images are from http://www.sasclouds.com/english/normal/. The Sentinel-2 data are downloaded from https://glovis.usgs.gov/. The research work also received technical support from European Space Agency (ESA) Network of Resources and used Sentinel Hub EO Browser (https://apps.sentinel-hub.com/eo-browser/) to access to Pléiades images. The SRTM DEM and ALOS DEM are available at https://earthexplorer.usgs.gov/ and https://www.eorc.jaxa.jp/ALOS/en/aw3d30/, respectively. The measured water level data are from Central Water Commission, India (http://cwc.gov.in/ffm_dashboard). The meteorological data are obtained from Meteoblue (https://www.meteoblue.com/en/weather/archive/export/30.390N79.720E), downloadable at http://doi.org/10.5281/zenodo.4978786. The on-site photos of the damaged hydropower stations are from https://www.sciencenews.org/article/india-glacier-flood-disaster-himalayas-uttarakhand. The simulation program EDDA, is available in the Supplement part at https://gmd.copernicus.org/articles/11/2841/2018/#section7.

Acknowledgment
This work was supported by the National Natural Science Foundation of China (Nos. 41941017 and U20A20112).

References

Allstadt, K. (2013). Extracting source characteristics and dynamics of the August 2010 Mount Meager landslide from broadband seismograms. *Journal of Geophysical Research-Earth Surface*, *118*, 1472–1490. https://doi.org/10.1002/jgrf.20110

Chen, H. X., & Zhang, L. M. (2015). EDDA 1.0: Integrated simulation of debris flow erosion, deposition and property changes. *Geoscientific Model Development*, *8*, 829–844. https://doi.org/10.5194/gmd-8-829-2015

Emergency Response Coordination Centre (ERCC) (2021). *European commission's directorate-general for european civil protection and humanitarian aid operations*. Retrieved from https://erccportal.jrc.ec.europa.eu/ercmaps/ECDM_20210208_India_Glacier_Floods.pdf

Farinotti, D., Huss, M., & Fürst, J. J. (2019). A consensus estimate for the ice thickness distribution of all glaciers on Earth. *Nature Geoscience*, *12*, 168–173. https://doi.org/10.1038/s41561-019-0300-3

Farinotti, D., Round, V., & Huss, M. (2019). Large hydropower and water-storage potential in future glacier-free basins. *Nature*, *575*, 341–344. https://doi.org/10.1038/s41586-019-1740-z

Grämiger, L. M., Moore, J. R., Gischig, V. S., Loew, S., Funk, M., & Limpach, P. (2020). Hydromechanical rock slope damage during late pleistocene and holocene glacial cycles in an alpine valley. *Journal of Geophysical Research: Earth Surface*. *125*, e2019JF005494. https://doi.org/10.1029/2019jf005494

Gruber, S., Hoelzle, M., & Haeberli, W. (2004). Permafrost thaw and destabilization of Alpine rock walls in the hot summer of 2003. *Geophysical Research Letters*, *31*, L13504. https://doi.org/10.1029/2004gl020051

Harris, I., Jones, P. D., Osborn, T. J., & Lister, D. H. (2014). Updated high-resolution grids of monthly climatic observations - The CRU TS3.10 dataset. *International Journal of Climatology*, *34*, 623–642. https://doi.org/10.1038/10.1002/joc.3711

Immerzeel, W. W., Van Beek, L. P. H., & Bierkens, M. F. P. (2010). Climate change will affect the Asian water towers. *Science*, *328*, 1382–1385. https://doi.org/10.1126/science.1183188

IPCC (2013). *Climate change 2013: The physical science basis. Contribution of working group I to the fifth assessment report of the intergovernmental panel on climate change*. Retrieved from https://www.ipcc.ch/report/ar5/wg1/

IPCC (2019). High mountain areas. In *IPCC special report on the ocean and cryosphere in a changing climate*. Cambridge University Press. Retrieved from https://www.ipcc.ch/srocc

Kirschbaum, D., Kapnick, S. B., Stanley, T., & Pascale, S. (2020). Changes in extreme precipitation and landslides over high mountain Asia. *Geophysical Research Letters*, *47*(4), e2019GL085347. https://doi.org/10.1126/10.1029/2019GL085347

Kumar, V., Shukla, T., & Mehta, M. (2020). Glacier changes and associated climate drivers for the last three decades, Nanda Devi region, Central Himalaya, India. *Quaternary International*. https://doi.org/10.1016/j.quaint.2020.06.017

Martha, T. R., Roy, P., Jain, N., Kumar, K. V., Reddy, P. S., Nalini, J., et al. (2021). Rock avalanche induced flash flood on 07 February 2021 in Uttarakhand, India—A photogeological reconstruction of the event. *Landslides*. https://doi.org/10.1007/s10346-021-01691-9

Marzeion, B., Cogley, J. G., Richter, K., & Parkes, D. (2014). Attribution of global glacier mass loss to anthropogenic and natural causes. *Science*, *345*, 919–921. https://doi.org/10.1126/science.1254702

Meena, S. R., Bhuyan, K., Chauhan, A., & Singh, R. P. (2021). Snow covered with dust after Chamoli rockslide: Inference based on high-resolution satellite data. *Remote Sensing Letters*, *12*, 704–714. https://doi.org/10.1080/2150704x.2021.1931532

Meteoblue Weather Maps. (2021). Retrieved from https://www.meteoblue.com/en/weather/maps/30.391N79.722E4094_Asia/Calcutta#coords=10.87/30.4405/79.7327&map=precipitation~hourly-hourly~auto~sfc~none

Mitchell, T. D., & Jones, P. D. (2005). An improved method of constructing a database of monthly climate observations and associated high-resolution grids. *International Journal of Climatology*, *25*, 693–712. https://doi.org/10.1002/joc.1181

Pandey, P., Chauhan, P., & Bhatt, C. M. (2021). Cause and process mechanism of rockslide triggered flood event in Rishiganga and Dhauliganga river valleys, Chamoli, Uttarakhand, India using satellite remote sensing and in situ observations. *Journal of the Indian Society of Remote Sensing*, *49*, 1011–1024. https://doi.org/10.1007/s12524-021-01360-3

Pelto, M. (2021). *Potential preconditioning for landslide high 2020 glacier snow lines in rishi ganga basin, India 2020*. Retrieved from https://blogs.agu.org/fromaglaciersperspective/2021/02/09/potential-preconditioning-for-landslide-high-2020-glacier-snow-lines-in-rishi-ganga-basin-india-2020/

Rana, N., Sharma, S., & Sundriyal, Y. (2021). A preliminary assessment of the 7th February 2021 flashflood in lower Dhauli Ganga valley, Central Himalaya, India. *Journal of Earth System Science*. https://doi.org/10.1007/s12040-021-01608-z

Scherler, D., Bookhagen, B., & Strecker, M. R. (2011). Spatially variable response of Himalayan glaciers to climate change affected by debris cover. *Nature Geoscience*, *4*, 156–159. https://doi.org/10.1038/ngeo1068

Shen, P., Zhang, L., & Wong, H. F. (2020). Debris flow enlargement from entrainment: A case study for comparison of three entrainment models. *Engineering Geology*, *270*, 105581.

Shrestha, A. B., Steiner, J., Nepal, S., Maharjan, S. B., Jackson, M., Rasul, G., & Bajracharya, B. (2021). *Understanding the Chamoli flood: Cause, process, impacts, and context of rapid infrastructure development*. Retrieved from https://www.icimod.org/article/understanding-the-chamoli-flood-cause-process-impacts-and-context-of-rapid-infrastructure-development/

Shugar, D. H., Jacquemart, M., Shean, D., Bhushan, S., Upadhyay, K., Sattar, A., et al. (2021). A massive rock and ice avalanche caused the 2021 disaster at Chamoli, Indian Himalaya. *Science*, *373*, 300–306. https://doi.org/10.1126/science.abh4455

Wang, Q., Yi, S., & Sun, W. (2021). Continuous estimates of glacier mass balance in high mountain Asia based on ICESat-1,2 and GRACE/GRACE follow-on data. *Geophysical Research Letters*, *48*, e2020GL090954. https://doi.org/10.1029/2020GL090954

Wang, W., Yang, J., & Wang, Y. (2020). Dynamic processes of 2018 Sedongpu landslide in Namcha Barwa–Gyala Peri massif revealed by broadband seismic records. *Landslides*, *17*, 409–418. https://doi.org/10.1007/s10346-019-01315-3

Watson, S. (2021). Retrieved from https://twitter.com/CScottWatson/status/1358692688946548737

Zemp, M., Huss, M., & Thibert, E. (2019). Global glacier mass changes and their contributions to sea-level rise from 1961 to 2016. *Nature*, *568*, 382–386. https://doi.org/10.1038/s41586-019-1071-0

Zhang, Z., He, S. M., & Liu, W. (2019). Source characteristics and dynamics of the October 2018 Baige landslide revealed by broadband seismograms. *Landslides*, *16*, 777–785. https://doi.org/10.1007/s10346-019-01145-3

Zhou, S. Y., Gao, L., & Zhang, L. M. (2019). Predicting debris-flow clusters under extreme rainstorms: A case study on Hong Kong Island. *Bulletin of Engineering Geology and the Environment*, *78*, 5775–5794. https://doi.org/10.1007/s10064-019-01504-3

References From the Supporting Information

Berthier, E., Cabot, V., Vincent, C., & Six, D. (2016). Decadal region-wide and glacier-wide mass balances derived from multi-temporal ASTER satellite digital elevation models. validation over the Mont-Blanc area. *Frontiers in Earth Science*. https://doi.org/10.3389/feart.2016.0006310.3389/feart.2016.00063

Chamoli disaster Feb 7 Summary of first insights (2021) *First insights into the Chamoli disaster, February 7 2021*. Retrieved from http://www.gaphaz.org/files/210220Update_Chamoli-disaster_20210207_GAPHAZ.pdf

Entwisle, D., Lee, K. A., & Lawley, R. S. (2015). *User guide for 'BGS civils': A suite of engineering properties datasets*. Nottingham, UK: British Geological Survey. Retrieved from http://nora.nerc.ac.uk/id/eprint/513379/

Graf, W. H. (1984). *Hydraulics of sediment transport*. Colorado: Water Resources Publications. https://doi.org/10.5772/25982

Hanson, G. J., & Simon, A. (2001). Erodibility of cohesive streambeds in the loess area of the midwestern USA. *Hydrological Processes*, *15*(1), 23–38. https://doi.org/10.1002/hyp.149

Jacquemart, M., Loso, M., Leopold, M., Welty, E., Berthier, E., Hansen, J. S. S., et al. (2020). What drives large-scale glacier detachments? Insights from flat creek glacier, St. Elias Mountains, Alaska. *Geology*, *48*(7), 703–707. https://doi.org/10.1130/G47211.1

Julien, P. Y., & Lan, Y. (1991). Rheology of hyper concentrations. *Journal of Hydraulic Engineering*, *117*(3), 346–353. https://doi.org/10.1061/(ASCE)0733-9429(1991)117:3(346)

Miles, E. S., Watson, C. S., & Brun, F. (2018). Ablative and geomorphic effects of a supraglacial lake drainage and outburst event, Nepal Himalaya. *The Cryosphere Discussions*, 1–25. https://doi.org/10.5194/tc-2018-152

Takahashi, T., Nakagawa, H., Harada, T., & Yamashiki, Y. (1992). Routing debris flows with particle segregation. *Journal of Hydraulic Engineering*, *118*(11), 1490–1507. https://doi.org/10.1061/(ASCE)0733-9429(1992)118:11(1490)

Tapovan Vishnugad Hydroelectric Power Plant Uttarakhand. (2014). Retrieved from https://www.power-technology.com/projects/tapovan-vishnugad-hydroelectric-power-plant-uttarakhand/

Journal Pre-proof

A numerical model for cascading glacier mass flow analysis (GMFA): Erosion-deposition dynamics, phase changes, and multi-hazard chain transformations

Ruochen Jiang, Limin Zhang, Wenjun Lu, Dalei Peng, Xin He, Shihao Xiao, Mingdong Wei

PII: S1674-7755(25)00154-4

DOI: https://doi.org/10.1016/j.jrmge.2025.02.010

Reference: JRMGE 2006

To appear in: *Journal of Rock Mechanics and Geotechnical Engineering*

Received Date: 6 November 2024

Revised Date: 12 February 2025

Accepted Date: 17 February 2025

Please cite this article as: Jiang R, Zhang L, Lu W, Peng D, He X, Xiao S, Wei M, A numerical model for cascading glacier mass flow analysis (GMFA): Erosion-deposition dynamics, phase changes, and multi-hazard chain transformations, *Journal of Rock Mechanics and Geotechnical Engineering*, https://doi.org/10.1016/j.jrmge.2025.02.010.

A numerical model for cascading glacier mass flow analysis (GMFA): Erosion-deposition dynamics, phase changes, and multi-hazard chain transformations

Ruochen Jiang[1], Limin Zhang[1, 2, *], Wenjun Lu[3], Dalei Peng[4], Xin He[1], Shihao Xiao[1], Mingdong Wei[5]

[1] Department of Civil and Environmental Engineering, The Hong Kong University of Science and Technology, Hong Kong, China
[2] HKUST Shenzhen-Hong Kong Collaborative Innovation Research Institute, Futian, Shenzhen, China
[3] Department of Civil and Environmental Engineering, Harbin Institute of Technology (Shenzhen), Shenzhen, China
[4] State Key Laboratory of Geo-Hazard Prevention and Geoenvironment Protection, Chengdu University of Technology, Chengdu, China
[5] State Key Laboratory of Hydraulics and Mountain River Engineering, College of Water Resource and Hydropower, Sichuan University, Chengdu, 610065, China

* Corresponding author. E-mail address: cezhangl@ust.hk (Limin Zhang)

Abstract: Glacier landslide cascading hazards pose threats to communities and infrastructure, affected by complex processes including the amplification of mass flow volume through erosion and entrainment, transformation of hazard types, ice-water phase change, and enhanced mobility of the mass flow. Scientifically simulating these physical phenomena proves challenging. This study introduces GMFA (glacier mass flow analysis), an integrated numerical model that advances the field by: (1) proposing depth-averaged fluctuation energy and internal energy equations, (2) incorporating the ice-water phase change and the entrainment-deposition process, and (3) capturing their effects on mass flow runout characteristics. The model employs the finite volume method to solve the multi-physics coupled governing equations, enabling efficient large-scale simulations. The model is verified through three numerical tests covering flow dynamics, temperature evolution, and thermo-hydro-mechanical runout processes. The model is applied to analyze a hazard chain that occurred on 10 September 2020 on the Tibetan Plateau. The multi-scenario simulation results indicate an entrained mass volume of $(4.95 \pm 0.11) \times 10^5$ m^3, and a ratio of entrained mass volume to source material volume of 0.44. The solid concentration decreases from 0.6–0.7 to 0.1–0.15 with increasing runout distance, indicating a transition from avalanche to debris flood. The internal energy rises by $(3–4) \times 10^3$ kJ/m^3, driving rapid ice melting from 0.1–0.2 to near-zero concentration. The model effectively quantifies volume amplification, ice-water phase changes, and multi-hazard transformations. This model pushes the geoscience frontier, extending computational capability from single- to multi-hazard simulations and providing a powerful tool for analyzing glacier cascading hazards.
Keywords: Glacier hazard chains; Landslides; Debris flows; Phase change; Erosion and deposition; Hazard transformation

1 Introduction

The global average surface temperature has risen over the past decades due to climate warming (0.16 ℃/decade) (Hugonnet et al., 2021; Wei et al., 2023; Jiang et al., 2024). Consequently, glacier detachments and frozen slope failures have become more frequent, resulting in glacier hazards in various locations (Millan et al., 2022; Yin et al., 2023; Xu et al., 2024), such as Yigong Gully (Xu et al., 2012; Delaney et al., 2015), Aru Glacier (Kääb et al., 2018; Wei et al., 2024), Sedongpu Glacier (Chen et al., 2020), Flat Creek Glacier (Jacquemart et al., 2020), and the Chamoli area (Jiang et al., 2021) (Fig. 1). The formed mass flows, composed of a mixture of rock/soil, water, and ice, are characterized by large volumes ($> 1 \times 10^6$ m^3) and long runout distances over 8 km (Fig. 1). These hazards pose escalating threats to both communities and infrastructure in alpine regions (Mani et al., 2023). An example is the rock-ice hazards that occurred in India's Chamoli district, on February 7th, 2021. This event caused severe damage to two hydropower stations and tragically claimed over 200 lives (Jiang et al., 2021) (Fig. 1).

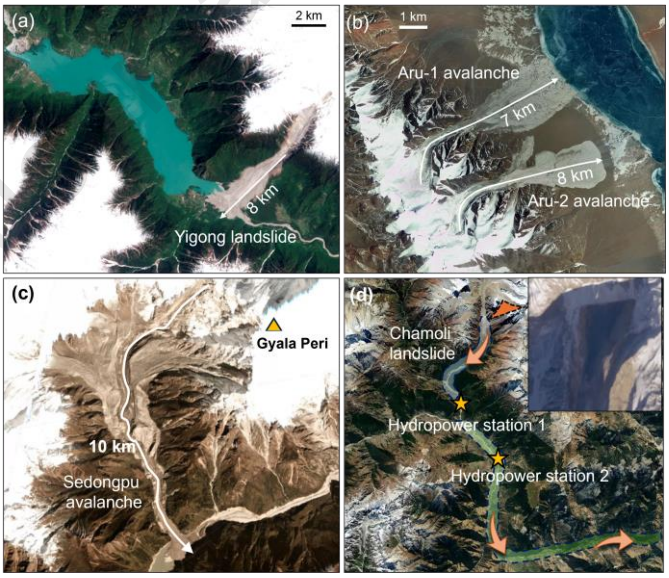

Fig. 1. Historical rock-ice cascading hazards: (a) The 2000 Yigong rock-ice landslide hazard chain, (b) The 2016 two Aru glaciers detachment hazard chains, (c) The 2018 Sedongpu debris-ice avalanche hazard chain, and (d) The 2021 Chamoli rock-ice landslide hazard chain.

Cascading propagation stands as a defining characteristic of rock-ice mass flows, illustrating their distinct nature and behavior (Mani et al., 2023; Jiang et al., 2021; Zhao et al., 2024). As shown in Fig. 2, a cascade starts from a rock-ice landslide, or a glacier collapse in a cold high mountain (>4000 m above sea level (a.s.l.)). The detached rock/ice mass disintegrates, leading to the formation of a rock-ice avalanche. As the mass flow progresses, it undergoes significant volume amplification and experiences multi-hazard transformations, transitioning from an avalanche to a debris flow or even a debris flood. This transformation occurs due to basal erosion, entrainment, mass deposition, or ice melting along its propagation path (Evans and Delaney, 2015; Jiang et al., 2021; Xiao et al., 2024). Consequently, the final mass volume can become several times greater than the initial volume. For instance, in the case of the Yigong landslide in 2000, the initial mass had a volume of 30×10^6 m^3. However, as it traveled a distance of 8 km, the accumulated deposit reached a remarkable final volume of 300×10^6 m^3 (Xu et al., 2012; Delaney et al., 2015). Another notable example is the 2021 Chamoli hazard, where a rock-ice avalanche transformed into a debris flow and finally a debris flood that traveled over 150 km in 24 h (Jiang et al., 2021; Siddique et al., 2022). Throughout the entire propagation process, significant changes occurred not only in the volume, velocity, and depth of the mass flow but also in

the properties of the mixture consisting of rock, ice, and water. These substantial changes directly influence the volume and mobility of the hazard (Chen et al. 2015; Mani et al., 2023).

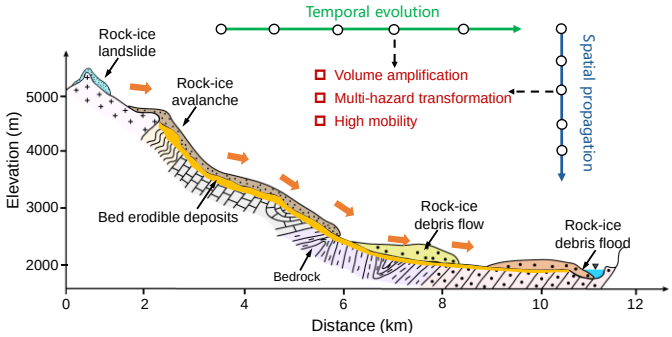

Fig. 2. Spatiotemporal evolution of rock-ice cascading hazards in mountain cryosphere.

The analysis of cascading hazards has attracted substantial attention from the scientific community. Takahashi et al. (1992) and Hungr (1995) have demonstrated that the volumetric sediment concentration, which is the proportion of solid volume to the total volume of the debris flow mixture, can undergo significant changes. These changes can occur through the entrainment of solid materials (Egashira et al., 2001; Iverson et al., 2011, 2012), or through processes such as deposition, as observed by Pierson and Scott (1985) and Takahashi et al. (1992). Accordingly, the rheological characteristics of mass flows vary in relation to the volumetric sediment concentration, as observed in numerous experiments (Sosio and Crosta, 2009; Bisantino et al., 2010). Some studies further investigated the effects of ice on the propagation of cascading hazards. Sansone et al. (2021) summarized key physical properties of rock-ice mass flows and emphasized the distinct characteristics attributed to ice melting in comparison to other geophysical flows. Feng et al. (2023) analyzed rock-ice avalanches and demonstrated that ice particles with smaller friction angles led to long-runout propagation. Ren et al. (2021) demonstrated, through small-scale experiments, that the ice content plays a crucial role in the movement of rock-ice avalanches due to ice melting. Similarly, Sosio et al. (2012) conducted back analyses of several documented cases, revealing a low apparent friction coefficient.

Several models have been developed for landslide mobility analysis (e.g. Takahashi et al., 1992; McDougall and Hungr, 2005; Hungr and McDougall, 2009; Ouyang et al., 2013). Some key physical processes have been integrated into these models. Medina et al. (2008) and Quan Luna et al. (2012) adopted the Mohr-Coulomb failure criterion to simulate channel bed erosion. Various rheological models have been utilized to characterize the behavior of mass flows. Examples of these models include the laminar flow model, the Bingham fluid model, and the Voellmy model (e.g. Fraccarollo and Papa, 2000; Takahashi, 2007; Medina et al., 2008). Pudasaini and Krautblatter (2014) and Pudasaini and Mergili (2019) developed powerful multi-phase flow models taking into account thermal effects implicitly based on flow velocity. Various numerical methods have been utilized to solve key governing equations, including the finite volume method (e.g. Medin et al., 2008; Xia et al., 2023), the finite difference method (e.g. Takahashi et al., 1992; Ouyang et al., 2013; Chent et al., 2015), and the smoothed particle hydrodynamics method (e.g. Goodwin and Choi, 2022). Several computer programs have been therefore developed, such as FLO-2D (O'Brien et al., 1993), DAN (Hungr, 1995), TOCHNOG (Crosta et al., 2003), FLATModel (Medina et al., 2008), DAN3D (Hungr and McDougall, 2009), MassMov2D (Beguería et al., 2009), RAMMS (Bartelt et al., 2013), EDDA (Chen et al., 2015; Shen et al., 2018), Massflow (Ouyang et al., 2013), and r.avaflow (Mergili et al., 2017).

Many of the above computational tools simulate one particular type of landslide hazard. Yet a landslide cascade shown in Figs. 1 and 2 involve multiple types of hazards in a sequence. Several key scientific problems remain unsolved in simulating the cascade processes in one go:

(1) How can the spatiotemporal transformation of multiple hazards in a hazard chain process be quantified (e.g. avalanche - debris flow - debris flood)?
(2) How can the ice-water phase change and the thermal state be explicitly quantified?
(3) How do the properties of mass flows (e.g. rheology, volume and mobility) evolve in the entrainment-deposition and ice melting processes?

This paper presents an integrated numerical model for glacier cascading hazards incorporating complex processes including erosion/entrapment-deposition, ice-water phase change, energy evolution, and variations in mechanical properties. Such an integrated model will extend our computational capability from single-hazard simulation to multi-hazard simulation. The results from the model can be utilized to analyze volume amplification, multi-hazard transformation, and the high mobility of glacier cascading hazards.

This paper is organized as follows. Section 2 introduces the framework, including problem description, governing equations, constitutive models, erosion/entrainment-deposition models, and numerical solutions. Section 3 rigorously tests and verifies the proposed model. A large-scale hazard event in Southeast Tibet is simulated as a field application in Section 4. Sections 5 and 6 provide a discussion of the main findings and a summary of the conclusions, respectively.

2 Framework and methodology

This section aims to present the physical characteristics of glacier landslide hazard chains and to introduce the governing equations that describe their associated dynamics and properties. Fig. 3 shows typical geo-materials and physical processes during the propagation of a mass flow. The motion characteristics, e.g. velocity and depth of flow, are described and quantified via mass and momentum conservation equations. The flowing mass consists of ice, water, and soil/rock, and therefore, mass conservation equations are needed to quantify the evolution of mass compositions. Variations in mass concentration can significantly influence the flow characteristics throughout the entire propagation process. With increasing solid concentration, the flow mass can transition through various hazard types, including an avalanche, a viscous debris flow, a diluted debris flow and a debris flood (Fig. 4). Consequently, the mechanical properties of the flowing mass undergo changes, e.g. rheological properties, which subsequently result in the spatiotemporal evolution of the dynamic characteristics of the flowing mass. These variations are attributed to the ice-water phase change and erosion/entrainment-deposition processes (Fig. 3). To accurately capture these phenomena, we have utilized a set of energy equations, erosion/entrainment-deposition equations, and flow resistance equations.

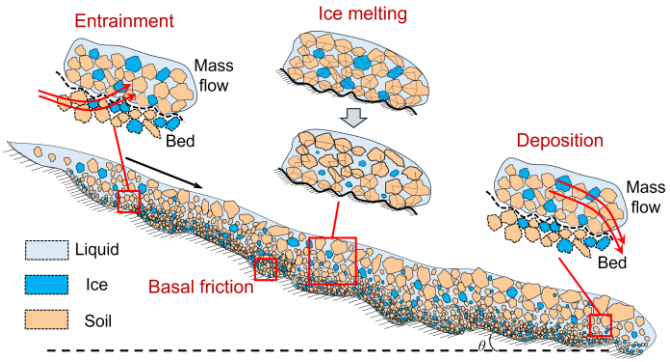

Fig. 3. Erosion/entrainment, deposition, ice melting and property changes during the propagation of debris-ice mass flows.

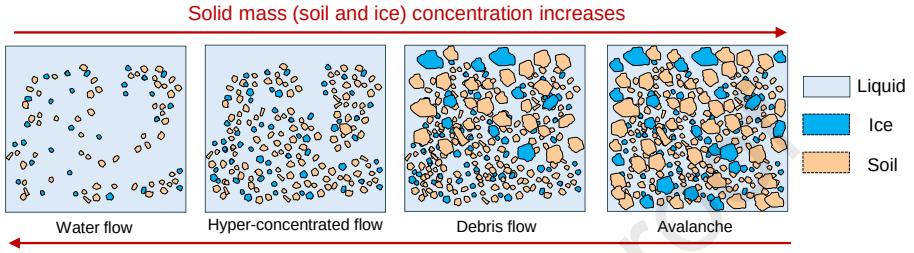

Fig. 4. Changes of volumetric sediment concentration in a debris-ice flow.

The proposed simulation model in this study captures and quantifies the physical processes based on the following assumptions:

(1) The flowing mass is a mixture composed of ice, water and soil/rock.
(2) The flowing mixture is considered as an equivalent fluid.
(3) The mass and momentum conservation of flowing mass can be described using shallow water equations.
(4) When the basal material is eroded by the overtopping mass flow, the failure of the stationary channel deposits in the channel (i.e. critical erosive shear stress) can be described by the Mohr-Coulomb criterion.

Based on these assumptions, this section is organized as follows. Section 2.1 introduces mass (i.e. rock/soil, water, and ice) and momentum conservation equations for the formed mass flow considering ice-water phase change and erosion/entrainment-deposition. Sections 2.2 and 2.3 are intended to analyze the phenomena associated with ice-water phase change and erosion/entrainment-deposition processes, respectively. To quantify the amount of ice-water phase change, we employ energy equations to track the evolution of both fluctuation energy (e.g. random kinetic energy) and internal energy (Section 2.2). In Section 2.3, we introduce the equations governing erosion/entrainment-deposition for the flowing mixture, which quantify variations in mass volume and concentration. In Section 2.4, we present equations that govern the rheological behaviors and flow resistances of the flowing mixture, both of which undergo changes in the cascading process. All governing equations will be summarized and reformulated in matrix form in Section 2.5, and the numerical strategies employed to solve the governing equations are detailed in Section 2.6. The finite volume method is adopted to solve the governing equations. By incorporating these modules, the complex interplay between mass, momentum, and energy in rock-ice mass flows can be captured. The subsequent sections of the paper present the governing equations, numerical solutions, validation and application of the proposed model.

2.1 Mass and momentum equations

The two-dimensional (2D) shallow water equations (SWEs) are widely utilized for modeling surface flows such as flash floods and debris flows, assuming a significant difference between the horizontal and vertical dimensions. These equations can also be adapted to simulate mass flows by incorporating erosion-deposition processes and accounting for volumetric changes in sediments (Ouyang et al., 2013; Chen et al., 2015; Xia et al., 2023). By integrating these processes into the SWEs, the model can capture the dynamic propagation of mass flows:

$$\frac{\partial(h)}{\partial t}+\frac{\partial(hu)}{\partial x}+\frac{\partial(hv)}{\partial y}=i\left[C_{v*}+\left(1-C_{v*}\right)s_b\right] \tag{1}$$

$$\frac{\partial(C_{vs}h)}{\partial t}+\frac{\partial(C_{vs}hu)}{\partial x}+\frac{\partial(C_{vs}hv)}{\partial y}=iC_{vs*} \tag{2}$$

$$\frac{\partial(C_{vi}h)}{\partial t}+\frac{\partial(C_{vi}hu)}{\partial x}+\frac{\partial(C_{vi}hv)}{\partial y}=iC_{vi*}-\frac{\partial(h_{wm})}{\partial t} \tag{3}$$

$$\frac{\partial(hu)}{\partial t}+\frac{\partial(hu^2+0.5gh^2)}{\partial x}+\frac{\partial(huv)}{\partial y}=gh\left[-\mathrm{sgn}(u)S_{fx}-\frac{\partial(z_b)}{\partial x}\right]-ui\left[C_{v*}+\left(1-C_{v*}\right)s_b\right] \tag{4}$$

$$\frac{\partial(hv)}{\partial t}+\frac{\partial(huv)}{\partial x}+\frac{\partial(hv^2+0.5gh^2)}{\partial y}=gh\left[-\mathrm{sgn}(v)S_{fy}-\frac{\partial(z_b)}{\partial y}\right]-vi\left[C_{v*}+\left(1-C_{v*}\right)s_b\right] \tag{5}$$

$$\frac{\partial(h_{wm})}{\partial t}=\boldsymbol{F}\left(E_i,E_w,E_s\right) \tag{6}$$

$$i=\boldsymbol{G}\left(h,u,v,\boldsymbol{f}_{bed}\right) \tag{7}$$

$$S_f=\boldsymbol{H}\left(E_i,E_w,E_s,\boldsymbol{f}_{bed}\right) \tag{8}$$

Eqs. (1)-(3) delineate the evolution of total flow depth (h), as well as the depth of soil ($C_{vs}h$) and ice ($C_{vi}h$) within the flowing mixture. Eqs. (4) and (5) determine the velocity of the moving mixture (u and v). h, u, v, C_{vs} and C_{vi} are the variables to be solved. In these governing equations, t is the time; (x, y) defines the 2D Cartesian coordinates; h is the flow depth of the mixture; h_{wm} is the ice melting water depth; v_x and v_y are the flow velocities along the x- and y-directions, respectively; $i=-\partial z/\partial t$ indicates the erosion or deposition rate; z is the bed elevation; C_{vs} and C_{vi} are the volumetric ratio of

rock/soil and ice in the flowing mixture, respectively; C_{vs*} and C_{vi*} are the volume fractions of rock/soil and ice in the entrained materials along the erodible bed, respectively; s_b is the saturation degrees in the erodible bed; the sgn(·) represents a sgn function satisfying sgn(x)=1 (when x>0), sgn(x)=0 (when x=0) and sgn(x)=-1 (when x<0), which indicates that the resistance direction is opposite to the flow direction; S_{fx} and S_{fy} are the flow resistance slopes in the x- and y-directions, respectively; and C_v=C_{vs}+C_{vi} and C_{v*}=C_{vs*}+C_{vi*} are the solid volume fractions in the flowing mixture and the erodible bed, respectively.

S_f, i, and h_{wm} can be obtained based on Eqs. (6)-(8). $\boldsymbol{F}\left(E_i, E_w, E_s\right)$, $\boldsymbol{G}\left(h, u, v, \boldsymbol{f}_{bed}\right)$, and $\boldsymbol{H}\left(E_i, E_w, E_s, \boldsymbol{f}_{bed}\right)$ are three functions and indicate that the solutions of h_{wm}, i, and S_f are related to the specific energy of ice, water and soil (E_i, E_w, E_s), flow variables (h, u, v), and physical properties of bed materials ($\boldsymbol{f}_{bed}$). More model information about Eqs. (6)-(8) has been introduced in Sections 2.2, 2.3, and 2.4, respectively.

Following EDDA (Chen et al., 2015; Shen et al., 2018) and Flo-2D (Flo-2D Software Inc., 2009), the flow type is defined according to C_v as

(1) If C_v < 0.2, the flowing mixture can be regarded as a debris flood.
(2) If 0.2 < C_v < 0.4, the flowing mixture is a diluted debris flow.
(3) If 0.4 < C_v <0.55, the flowing mixture is a viscous debris flow.
(4) If 0.55 < C_v, the flowing mixture is an avalanche.

2.2 Internal energy equations

The heat exchange during erosion/entrainment-deposition, heat transfer with the ambient environment, and latent heat associated with ice-water phase change are considered. In the timescale of mass flow propagation, the contribution of diffusive heat transfer is relatively small (Bartelt et al., 2006; Valero et al., 2015). Therefore, only thermal heat advection is taken into account, while diffusive heat transfer is not modeled within the rock-ice mass flow. The thermal energy (internal energy) equation is expressed as follows:

$$\frac{\partial Eh}{\partial t}+\frac{\partial (Ehu)}{\partial x}+\frac{\partial (Ehv)}{\partial y}=\left(1-\alpha_E\right)\dot{W}+\beta_E RhC_v+\frac{\partial (E_{ED})}{\partial t}+L\rho_w\frac{\partial (h_{wm})}{\partial t}+k\left(T_{amb}-T\right) \tag{9}$$

where E is the specific internal energy; and $\partial(E_{ED})/\partial t$ represents the erosion/entrainment-deposition heat, which can be written as

$$\frac{\partial (E_{ED})}{\partial t}=\begin{cases}\rho_{bed}C_{bed}T_{bed}i & (i>0)\\ \rho C_f T_f i & (i<0, C_v>0)\end{cases} \tag{10}$$

where C_{bed} and C_f are the specific heat capacities of the bed material and the flowing mass, respectively; T_{bed} and T_f denote the temperatures of the bed material and the flowing mass, respectively; $L\rho_w\partial(h_{wm})/\partial t$ reflects the latent heat of ice-water phase change, in which L is the specific latent heat of ice (334 kJ/kg) and h_{wm} is the meltwater depth per unit area resulting from ice-water phase change; k is the heat transfer coefficient; and T and T_{amb} are the flowing mass temperature and the ambient temperature, respectively.

In Eq. (9), α_E represents the production rate of random fluctuation energy (i.e. random particle kinetic energy) resulting from the shear work rate $\dot{W}$. When α_E =0, all friction work is dissipated to heat, and friction shearing does not generate any fluctuation energy in the mass flow. If α_E >0, friction shearing produces fluctuation energy, but inelastic interaction of granular particles causes the fluctuation energy to decay at a rate β_E (Buser and Bartelt, 2009). All fluctuation energy will eventually dissipate as heat. 1– α_E and β_E therefore represent the heat production by friction shearing and decay of fluctuation energy, respectively.

Given the presence of ice, rock/soil, and water in rock-ice mass flows, we utilize three separate internal energy equations to describe the variations in their internal energy:

$$\begin{aligned}&\frac{\partial \left(E_i h\right)}{\partial t}+\frac{\partial (E_i hu)}{\partial x}+\frac{\partial (E_i hv)}{\partial y}=\frac{C_{vi}}{C_{vi}+C_{vs}}\left(1-\alpha_E\right)\dot{W}+\beta_E RhC_{vi}\\ &+\frac{\partial (E_{ED}C_{vi*})}{\partial t}+L\rho_w\frac{\partial (h_{wm})}{\partial t}+k_{i,amb}\left(T_{amb}-T_i\right)+k_{i,w}\left(T_w-T_i\right)+k_{i,s}\left(T_s-T_i\right)\end{aligned} \tag{11}$$

$$\begin{aligned}&\frac{\partial \left(E_s h\right)}{\partial t}+\frac{\partial (E_s hu)}{\partial x}+\frac{\partial (E_s hv)}{\partial y}=\frac{C_{vs}}{C_{vi}+C_{vs}}\left(1-\alpha_E\right)\dot{W}+\beta_E RhC_{vs}\\ &+\frac{\partial (E_{ED}C_{vs*})}{\partial t}+k_{s,amb}\left(T_{amb}-T_s\right)+k_{s,w}\left(T_w-T_s\right)+k_{s,i}\left(T_i-T_s\right)\end{aligned} \tag{12}$$

$$\begin{aligned}&\frac{\partial \left(E_w h\right)}{\partial t}+\frac{\partial (E_w hu)}{\partial x}+\frac{\partial (E_w hv)}{\partial y}=\frac{\partial (E_{ED}C_{vw*})}{\partial t}\\ &+k_{w,amb}\left(T_{amb}-T_w\right)+k_{w,s}\left(T_s-T_w\right)+k_{w,i}\left(T_i-T_w\right)\end{aligned} \tag{13}$$

where E_j (j= s, w, i) are the specific internal energy of rock/soil, water and ice in the mass flow; T_j (j=amb, s, w, i) represent ambient, rock/soil, water and ice temperature; C_{vj*} (j=s, w, i) are volumetric ratios of rock/soil, water and ice of the bed geo-materials; and $k_{j,k}$ (j,k=amb, s, w, i)) is the heat transfer coefficient between the jth phase and the kth phase.

The kinetic energy of mass flows comprises both translational and random kinetic energy components. The translational kinetic energy accounts for the overall movement and velocity of the mass flow (i.e. u and v in Eqs. (2) and (3)), while the random kinetic energy represents the chaotic motion of particles within the flow (Fig. 5). The kinetic energy of the mass flow is subsequently dissipated. This energy conversion arises from internal friction and viscous forces acting within the flowing mixture. The heat generated is a consequence of the dissipative processes, signifying the conversion of mechanical energy into thermal energy within the mass flow. In this study, Eq. (14) is taken to solve the variable R in Eqs. (11)-(13). Eq. (14) is a depth-averaged energy equation accounting for the kinetic energy $R(x, y, t)$ associated with solid particle velocity fluctuations (Bartelt et al., 2006; Buser and Bartelt, 2009; Valero et al., 2015).

$$\frac{\partial \left(RhC_v\right)}{\partial t}+\frac{\partial (RhC_v u)}{\partial x}+\frac{\partial (RhC_v v)}{\partial y}=\alpha_E\dot{W}-\beta_E RhC_v \tag{14}$$

where R is the specific fluctuation energy of solid particles; and $\dot{W}$ is the frictional work rate, which can be written as

$$\dot{W}=\tau\sqrt{u^2+v^2} \tag{15}$$

The flow resistance S_f in Eqs. (4) and (5) decreases in response to the fluctuation energy change as (Valero et al., 2015):

$$S_f=S_{f0}\exp\left(-\frac{R}{R_0}\right) \tag{16}$$

where S_{f0} is the flow resistance slope excluding impacts resulting from the fluctuation energy, and R_0 is the activation energy (Bartelt et al., 2012).

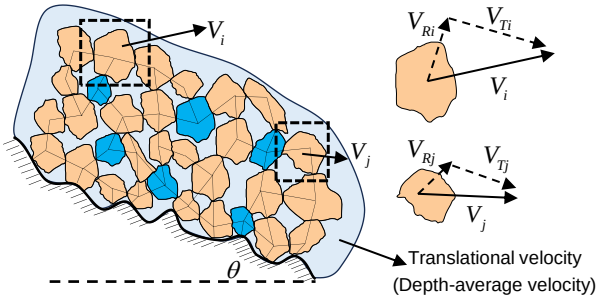

Fig. 5. Diagram of chaotic motion of particles (V_{Ri} and V_{Rj}) and translational velocity (V_{Ti} and V_{Tj}) of the *i*th and *j*th particles within the mass flow.

2.3 Erosion/entrainment and deposition

During the mass flows, erosion/entrainment and deposition processes can induce changes in mass volume and the volume ratios of rock, ice, and water. In this study, we adopt the Iverson model (Iverson and Ouyang, 2015):

$$i=\begin{cases} K_e \dfrac{\tau-\tau_c}{\rho_{bed}\sqrt{u^2+v^2}} & (\tau \geq \tau_c) \\ C_{dep} \dfrac{\tau-\tau_c}{\rho_{bed}\sqrt{u^2+v^2}} & (\tau < \tau_c) \end{cases} \tag{17}$$

in which ρ_{bed} is the bed material density, and the shear stress τ can be expressed as (Graf, 1984):

$$\tau=\rho g h S_f \tag{18}$$

where K_e and C_{dep} are the erosion and deposition coefficients, respectively. The values of these two parameters are determined based on field tests or historical case analysis. This formulation has been calibrated in various experiments. Moreover, by undergoing a mathematical transformation, the model can be transformed into other models, such as the Takahashi model (Takahashi et al., 1992) (Xia et al., 2023). The Iverson model has been adopted in several models, e.g. Xia et al. (2023), and Van Den Bout et al. (2022).

The interaction between the mass flows and the original deposits of rock and soil in the channel involves the interplay between the moving fluid (ice-rock-water mass flows) and the stationary solid materials (the original deposits in the valley channel). When the shear stress exerted by the flowing mass on the basal material exceeds the shear strength of the basal material, known as the critical erosive shear stress τ_c, the basal deposit becomes unstable and integrates into the flowing material. The erosion of bed deposits is considered as a Mohr-Coulomb failure process (Medina et al. 2008; Quan Luna et al. 2012), and the critical erosive shear stress τ_c is calculated using the following equation (Chen et al., 2015):

$$\tau_c = c_{bed} + C_v\left(\rho_s-\rho_w\right) g h \cos\theta \tan\phi \tag{19}$$

where c_{bed} is the effective cohesion of the bed material.

2.4 Rheological models

Constitutive models are required to accurately quantify S_f in the momentum equations (i.e. Eqs. (4) and (5)), which allow for the simulation of various types of flows. Rheological behavior of mass flows is an active research area. Many models are available, but in this section, for brevity, only two rheological models are introduced for calculating S_f, including the Voellmy model and the quadratic model.

The Voellmy model combines the effects of frictional and turbulent behavior and is utilized in the analysis of mass flow propagation (Voellmy, 1955):

$$S_f = \cos\theta \tan\phi + \frac{V^2}{\xi h} \tag{20}$$

where θ and ϕ are the bed slope and the friction angle of the solid particles contacting the bed, respectively; V and h are the flow velocity and the flow depth, respectively; and ξ is a turbulence parameter.

The quadratic rheological model proposed by Julien and Lan (1991) accounts for frictional and viscous behavior, turbulent effects, and resistance arising from solid-particle contacts:

$$S_f = \frac{\tau_y}{\rho g h} + \frac{K\mu V}{8\rho g h^2} + \frac{n_{td}^2 V^2}{h^{4/3}} \tag{21}$$

where the three terms on the right-hand side represent the flow resistance resulting from fluid yield stress, fluid viscous behavior, and turbulent effects, respectively; $V=\sqrt{u^2+v^2}$ is the absolute value of depth-averaged flow velocity; K is a laminar flow resistance coefficient; and n_{td}, τ_y and μ are the equivalent Manning coefficient of the mass flow, yield stress, and the dynamic viscosity, respectively, which are determined via the following equations (O'Brien & Julien, 1988):

$$n_{td} = 0.0538 n_m e^{6.0896 C_v} \tag{22}$$

$$\tau_y = \alpha_1 e^{\beta_1 C_v} \tag{23}$$

$$\mu = \alpha_2 e^{\beta_2 C_v} \tag{24}$$

where α_1, α_1, β_1 and β_2 are empirical parameters. When $C_v \leq 0.1$, τ_y is calculated as (Chen et al., 2015):

$$\tau_y = (1-C_s) C_v (\rho_s-\rho_w) g h \cos\theta^2 \tan\phi \tag{25}$$

where C_s is the coefficient of suspension of solid particles and $(1-C_s)$ is the solid portion that is in contact with erodible bed; θ is the slope angle; ρ_s and ρ_w are the densities of solids and water, respectively; and ϕ is the friction angle associated with the solid particles in contact with the bed.

2.5 Summary of governing equations

The governing equations can be organized as a system and expressed in a matrix form as follows:

$$\frac{\partial \boldsymbol{q}}{\partial t} + \frac{\partial \boldsymbol{F}_x}{\partial x} + \frac{\partial \boldsymbol{F}_y}{\partial y} = \boldsymbol{S} \tag{26}$$

where $\boldsymbol{q}$ represents all variables; $\boldsymbol{F}_x$ and $\boldsymbol{F}_y$ are the flux terms along the *x*- and *y*-directions, respectively; and $\boldsymbol{S}$ is the source term. These terms can be expressed as

$$\boldsymbol{q} = \begin{bmatrix} h & hC_{vs} & hC_{vi} & hu & hv & RhC_v & E_i h & E_s h & E_w h \end{bmatrix}^{\mathrm{T}} \tag{27}$$

$$\boldsymbol{F}_x = \begin{bmatrix} hu & huC_{vs} & huC_{vi} & hu^2 + 0.5gh^2 & huv & RhuC_v & E_i hu & E_s hu & E_w hu \end{bmatrix}^{\mathrm{T}} \tag{28}$$

$$\boldsymbol{F}_y = \begin{bmatrix} hv & hvC_{vs} & hvC_{vi} & huv & hv^2 + 0.5gh^2 & RhvC_v & E_i hv & E_s hv & E_w hv \end{bmatrix}^{\mathrm{T}} \tag{29}$$

$$\boldsymbol{S} = \begin{bmatrix} i\left[C_{v^*} + (1 - C_{v^*})s_b\right] \\ iC_{vs^*} \\ iC_{vi^*} - \dfrac{\partial(h_{wm})}{\partial t} \\ gh\left[-\mathrm{sgn}(u)S_{fx} - \dfrac{\partial(z_b)}{\partial x}\right] - ui\left[C_{v^*} + (1 - C_{v^*})s_b\right] \\ gh\left[-\mathrm{sgn}(u)S_{fy} - \dfrac{\partial(z_b)}{\partial y}\right] - vi\left[C_{v^*} + (1 - C_{v^*})s_b\right] \\ \alpha_E \dot{W} - \beta_E RhC_v \\ \dfrac{C_{vi}}{C_{vi} + C_{vs}}(1 - \alpha_E)\dot{W} + \beta_E RhC_{vi} + \dfrac{\partial(E_{ED}C_{vi^*})}{\partial t} + L\rho_w \dfrac{\partial(h_{wm})}{\partial t} + k_{i,amb}(T_{amb} - T_i) + k_{i,w}(T_w - T_i) + k_{i,s}(T_s - T_i) \\ \dfrac{C_{vs}}{C_{vi} + C_{vs}}(1 - \alpha_E)\dot{W} + \beta_E RhC_{vs} + \dfrac{\partial(E_{ED}C_{vs^*})}{\partial t} + k_{s,amb}(T_{amb} - T_s) + k_{s,w}(T_w - T_s) + k_{s,i}(T_i - T_s) \\ \dfrac{\partial(E_{ED}C_{vw^*})}{\partial t} + k_{w,amb}(T_{amb} - T_w) + k_{w,s}(T_s - T_w) + k_{w,i}(T_i - T_w) \end{bmatrix} \tag{30}$$

2.6 Numerical solution algorithm

In solving the governing equation system (Eq. (30)), the first step is to discretize the calculation domain into a finite number of cells. Once the domain is discretized, the initial flow velocity can be projected onto the *x*- and *y*-axis directions within each cell. Each cell is assigned specific physical properties, such as initial flow depth and flow velocity. Then, Eq. (30) is divided into two one-dimensional problems along the *x*- and *y*-direction, respectively (Ouyang et al., 2013):

$$\boldsymbol{q}_j^{n+1} = \boldsymbol{q}_j^n - \frac{\Delta t}{A_{cell}} \sum_{k=1}^{N} \boldsymbol{F}_k\left(\boldsymbol{q}_j^n\right) l_k + \Delta t \boldsymbol{S}^n \tag{31}$$

where n is the time step, Δt is the interval between two time steps, A_{cell} is the cell area, j is the grid cell index, k indicates the index of cell edges, N is the total number of edges of a grid cell, l_k represents the edge length of the grid edge k, and $\boldsymbol{F}_k\left(\boldsymbol{q}_j^n\right)$ represents the flux normal to the edge k of the cell j at the time step n.

The finite volume method (Rusanov, 1961) is adopted to explicitly calculate the flux terms and all variables. The Riemann state of flow depth should be defined. For the edge shared by two adjacent cells (e.g. the updating cell j and its neighbour j+1) (Fig. 6), the reconstructed elevations of mass flow surface can be expressed as

$$\left.\begin{aligned} \eta_L &= \eta_j + \max\left[0, \min\left(z_{j+1} - z_j - (z_{j+1/2+} - z_{j+1/2-}), \eta_{j+1} - \eta_j\right)\right] \\ \eta_R &= \eta_{j+1} + \max\left[0, \min\left(z_j - z_{j+1} + (z_{j+1/2+} - z_{j+1/2-}), \eta_j - \eta_{j+1}\right)\right] \end{aligned}\right\} \tag{32}$$

where η_j and η_{j+1} are the surface elevations of the flowing mass at the center of grid cells (j) and (j+1), respectively; $z_{j+1/2-}$ and $z_{j+1/2+}$ are the ground bed elevations at the left and right boundaries of the shared edge (j+1/2), which are interpolated from the corresponding cell-centre values using a slope limited method.

$$\left.\begin{aligned} z_{j+1/2-} &= z_j + \boldsymbol{r}_j \nabla z_j \\ z_{j+1/2+} &= z_{j+1} + \boldsymbol{r}_{j+1} \nabla z_{j+1} \end{aligned}\right\} \tag{33}$$

where **r** represents the vector extending from the cell center to the cell edge, while ∇z denotes the slope-limited gradient. In this study, the minmod slope limiter is employed (Velechovsky et al., 2019). The Riemann states of flow depth are defined as

$$\left.\begin{aligned} h_L &= \max\left(0, \eta_L - \max(z_j, z_{j+1})\right) \\ h_R &= \max\left(0, \eta_R - \max(z_j, z_{j+1})\right) \end{aligned}\right\} \tag{34}$$

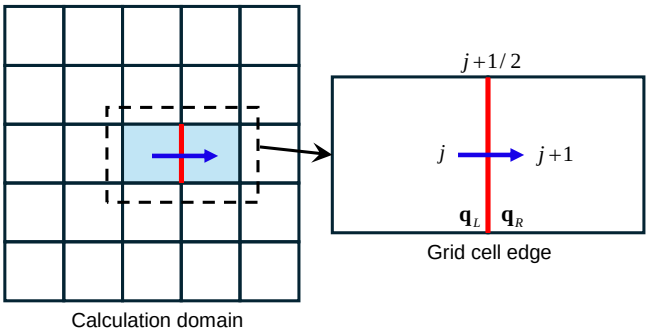

Fig. 6. Definition of local Riemann states.

The Riemann states of other variables can be expressed as

$$\left.\begin{array}{llll} (hC_{vs})_L = h_L C_{vs,j} & (hu)_L = h_L u_j & (hRC_v)_L = h_L R_j C_{v,j} & (E_s h)_L = h_L E_{s,j} \\ (hC_{vs})_R = h_R C_{vs,j+1} & (hu)_R = h_R u_{j+1} & (hRC_v)_R = h_R R_{j+1} C_{v,j+1} & (E_s h)_R = h_R E_{s,j+1} \\ (hC_{vi})_L = h_L C_{vi,j} & (hv)_L = h_L v_j & (E_i h)_L = h_L E_{i,j} & (E_w h)_L = h_L E_{w,j} \\ (hC_{vi})_R = h_R C_{vi,j+1} & (hv)_R = h_R v_{j+1} & (E_i h)_R = h_R E_{i,j+1} & (E_w h)_R = h_R E_{w,j+1} \end{array}\right\} \quad (35)$$

Once the Riemann variables are obtained, the fluxes can be subsequently calculated by the HLLC Riemann solver (Toro, 2001; Xia et al., 2023). Taking the *x*-direction as an example (Fig. 6), the flux at the edge (*j*+1/2) between cell *j* and cell *j*+1 can be expressed as follows:

$$\boldsymbol{F}\left(\boldsymbol{q}^n_{j+\frac{1}{2}}\right) = \frac{\boldsymbol{F}\left(\boldsymbol{q}^n_L\right) + \boldsymbol{F}\left(\boldsymbol{q}^n_R\right)}{2} + \max\left\{ r\left(\frac{\partial \boldsymbol{F}\left(\boldsymbol{q}^n_L\right)}{\partial \boldsymbol{q}}\right),\ r\left(\frac{\partial \boldsymbol{F}\left(\boldsymbol{q}^n_R\right)}{\partial \boldsymbol{q}}\right)\right\} \cdot \frac{\boldsymbol{q}^n_L - \boldsymbol{q}^n_R}{2} \quad (36)$$

where $\boldsymbol{F}\left(\boldsymbol{q}^n_{j+1/2}\right)$ is the normal flux through the edge (*j*+1/2) at time step *n*; $\boldsymbol{F}\left(\boldsymbol{q}^n_L\right)$ and $\boldsymbol{F}\left(\boldsymbol{q}^n_R\right)$ are the normal flux along the *x*-direction at the left and right boundaries of the shared edge (*j*+1/2), respectively; $\partial \boldsymbol{F}\left(\boldsymbol{q}^n_L\right)/\partial \boldsymbol{q}$ and $\partial \boldsymbol{F}\left(\boldsymbol{q}^n_R\right)/\partial \boldsymbol{q}$ are the Jacobian matrices of $\boldsymbol{F}\left(\boldsymbol{q}^n_L\right)$ and $\boldsymbol{F}\left(\boldsymbol{q}^n_R\right)$ with respect to all variables, respectively; and $r\left(\partial \boldsymbol{F}\left(\boldsymbol{q}^n\right)/\partial \boldsymbol{q}\right)$ represents the spectral radius of $\partial \boldsymbol{F}\left(\boldsymbol{q}^n\right)/\partial \boldsymbol{q}$. By utilizing the same approach, we can calculate the normal flux for all edges of each cell and subsequently update all variables in Eq. (30) in the discretized domain at the next time step.

To calculate the meltwater production in the mass flow (i.e. h_{wm}), a phase-change constraint criterion is adopted. The ice temperature in the mass flow can be calculated as

$$T_i = \frac{E_i}{\rho_i C_i} \quad (37)$$

where C_i is the specific heat capacity of ice mass. To update the ice temperature in the mass flow from time step *n* to time step *n*+1, the following process is adopted (Fig. 7):

(1) Obtain the ice temperature T_i^n and specific internal energy E_i^n at time step *n*, and T_i^n must satisfy $T_i^n \le 0$ °C.

(2) Calculate the temperature (T_i^{n+1}) and specific internal energy (E_i^{n+1}) at time step *n* + 1.

(3) Check if E_i^{n+1} exceeds specific internal energy E_m (i.e. specific internal energy of ice mass when the ice temperature is equal to the melting temperature, T_m), adjust the ice temperature to T_m, and limit the specific internal energy of ice mass to E_m. The meltwater production in this time step can be quantified as

$$\Delta h_{wm} = \frac{E_i^{n+1} - E_m}{L\rho_w} \quad (38)$$

Given that the calculation of the meltwater volume in each cell affects other variables, a sequential updating scheme is implemented to ensure proper coupling of the solution variables at each time step (Fig. 8). First, we solve governing equations involving flow depth and momentum (Eqs. (1), (4), and (5)). Next, we proceed to address the energy equations (Eqs. (11)-(14)). Finally, we update all variables related to the mass volume ratios (Eqs. (2) and (3)).

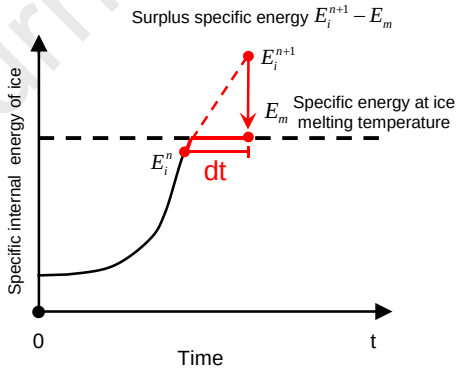

Fig. 7. Process of quantifying ice-melting water.

To improve computational efficiency, updates are selectively performed for specific grid cells instead of all of them. We define h_t = 0.001 m as a threshold to determine whether the grid is dry or wet. When $h > h_t$ in the cell, all variables will be calculated; when $h < h_t$, only the flow depth will be updated. Furthermore, it is imperative to select an appropriately small time step to guarantee numerical stability when explicitly solving the depth-averaged differential equations. The calculation time step has to be restricted by the Courant-Friedrich-Levy (CFL) criterion:

$$\Delta t = CFL \cdot \min\left[\min_j\left(\frac{\Delta x}{|u_j| + \sqrt{g h_j}}\right), \min_j\left(\frac{\Delta y}{|v_j| + \sqrt{g h_j}}\right)\right] \quad (39)$$

where Δx and Δy are the grid cell sizes along *x*- and *y*-direction, respectively; *j* indicates the *j*th grid cell; and *CFL* is a dimensionless parameter, i.e. the courant number, ranging from 0 to 1. More details about the calculation process are presented in Fig. 8.

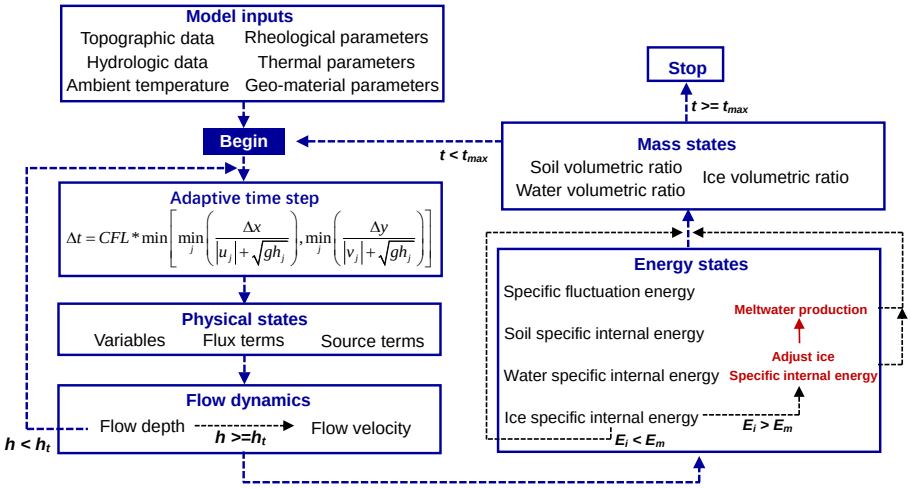

Fig. 8. Flow chart of the proposed simulation model.

3 Model verification

This section presents three numerical tests to verify the performance of the proposed framework. Test 1 demonstrates the application of the proposed framework in solving a 2D dam-breaching flow problem, ensuring that the computational model accurately captures the flow depth and velocity characteristics of the flowing mass. In test 2, we analyzed three rotating drum experiments in which the flow velocity and shearing forces were controlled. The temperature evolution of steadily flowing ice was measured in these experiments. This test is designed to validate the accuracy of the internal energy equation (temperature equation). In test 3, we analyze the deposition distribution and temperature changes following the movement of a soil-ice mass flow in a centrifuge experiment. Test 3 was designed to validate the reasonableness of the erosion-deposition equation and to assess the accuracy of the temperature calculation results when the mass and momentum conservation equations, and the internal energy equation are coupled.

3.1 Test 1: Dam-breaching water flow

The dam-breaching experiment conducted by Fennema and Hanif Chaudhry (1987) is adopted to verify mass and momentum conservation equations. The geometric features of the analysis domain are presented in Fig. 9a. The analysis area measures 200 m × 200 m, with a gray area in the center representing a dam that prevents water flow (Fig. 9a). On either side of the dam are reservoirs filled with water, with depths of 10 m and 5 m, respectively. In the experiment, a section of the dam failed instantaneously, resulting in a breach that was 75 m long.

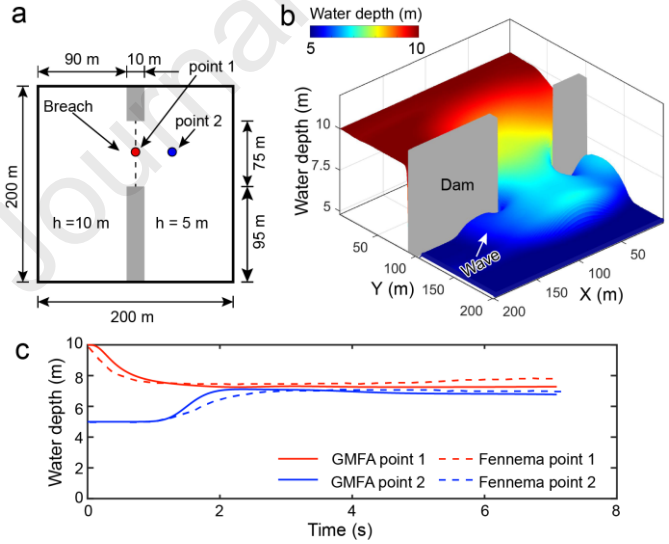

Fig. 9. Dam-breaching water flow analysis in Test 1: (a) Geometric features of the calculation domain, (b) Simulated water depth at 7.1 s after dam breaches calculated using the proposed model, and (c) Comparison of the computed water depths at selected points using the proposed model and results reported by Fennema and Hanif Chaudhry (1987).

We established a numerical model based on the experimental dimensions and initial water depths (Fig. 9b). The computational domain is discretized into grid cells with dimensions of 1 m × 1 m, and the calculation time step is set as 0.01 s, as reported in Chen et al. (2015). The flow resistance slope (i.e. S_f) is set as 0. All boundaries of the calculation domain are frictionless. Fig. 9b illustrates the water depth 7.1 s after the dam breaches, aligning with the results of Fennema and Hanif Chaudhry (1987). In Fig. 9a, two points are chosen to assess the temporal change in water depth over time.

The solid lines in Fig. 9c illustrate the trends of water depth changes over time at points 1 and 2. Owing to the initial hydraulic head difference between the upstream (left) and downstream (right) regions of the dam, a transient flow regime is established, characterized by a monotonic decrease in water depth at monitoring point 1 and a corresponding increase at monitoring point 2, consistent with the principles of mass conservation and hydraulic gradient-driven flow dynamics. As the water level difference between the two sides of the dam diminishes, the rates of water level decrease at point 1 and increase at point 2 both slow down until the water levels at both points stabilize. The dashed lines in Fig. 9c represent the numerical simulation results, which exhibit the same water depth evolution trends. The results obtained from the numerical solution using the proposed model agree well with the experimental results in Fig. 9b.

3.2 Test 2: Vertically rotating drum experiments

Three repeated rotating drum experiments conducted by Fischer et al. (2018) were used to validate the accuracy of the internal energy equation

(temperature equation), recording the temperature changes during the steady flow of ice. Fig. 10a and b shows the geometric features of the vertically rotating drum device. The drum, with a radius of r =1.23 m and a sectional width of 0.45 m, was rotated vertically at a constant angular velocity of ω = 0.25 s^{-1} (Fig. 10b). As the drum rotates, the ice particles maintain a steady flow at the bottom (Fig. 10a and b). With the drum's rotational speed remaining constant, the ice particles achieve a uniform motion velocity. In particular, the depth of the flowing ice was maintained at a constant value of h = 0.11 m. Throughout the experimental duration, a high-precision temperature sensor was strategically positioned within the drum's interior to continuously monitor and record the transient thermal characteristics of the mass flow, ensuring accurate temporal resolution of the phase change dynamics (Fig. 10a and b). During the steady flow process, the ambient temperatures (T_{amb}), initial temperatures (T_0), thermal equilibrium temperatures (T^*), heat transfer coefficient (K) and shear stress (τ) in these experiments were measured and are presented in Table 1. Table 1 shows initial ice temperatures (T_0 = -7.6 °C, -8.5 °C, and -7.7 °C) and initial ambient temperatures (T_{amb} = -4.6 °C, -4.8 °C, and -4.5 °C) in three repeated experiments. The measured heat transfer coefficients between the ice and the environment in the three repeated experiments were 224 J/(m^2 s °C), 228 J/(m^2 s °C), and 249 J/(m^2 s °C), respectively. The measured shearing stress values in these experiments were 107 Pa, 169 Pa, and 152 Pa.

Table 1. Measured parameters and average values in the physical experiments in Test 2 (Fischer et al., 2018).

Experiment	Ambient temperature, T_{amb} (°C)	Initial temperature, T_0 (°C)	Thermal equilibrium temperature, T^* (°C)	Heat transfer coefficient, K (J/(m^2 s °C))	Shear stress, τ (Pa)
1	-4.6	-7.6	-3.7	224	107
2	-4.8	-8.5	-3.3	228	169
3	-4.5	-7.7	-3.4	249	152

The proposed GMFA model in this study was taken to simulate the temperature changes of ice flows. Because the flowing mass is in a steady state, with constant flow depth and velocity, we take a flow depth of h = 0.11 m and a flow velocity of $v = r\,\omega$ = 1.23 m × 0.25 s^{-1} ≈ 0.3 m/s. Eq. (11) is taken to simulate the temperature changes of ice flows, in which the flux gradient terms were taken as 0 considering the steady flow state. The friction work rate on the right hand of Eq. (11) is calculated based on the measured shearing stress and the flow velocity (Eq. 15). Considering that the flowing mass is in a steady flow state, the fluctuation energy is assumed to be zero, and the relevant coefficients α_E and β_E are also set to zero. Only the heat exchange between the ice phase and the environment is considered, with the heat exchange coefficient taken from the empirical results presented in Table 1. Furthermore, the time step is set as 0.01 s.

Fig. 10c-e presents all measured and simulated temperature changes during the steady-state ice flow. The light blue and light red curves represent the measured original temperatures of the flowing ice and the ambient temperature during these experiments, respectively. The dashed curves in this figure represent the corresponding move-mean results. The black curve represents the simulation results, which indicates that the simulated results closely match the experimental results. This demonstrates that the proposed internal equation can accurately reflect the temperature changes of the flowing mass during motion.

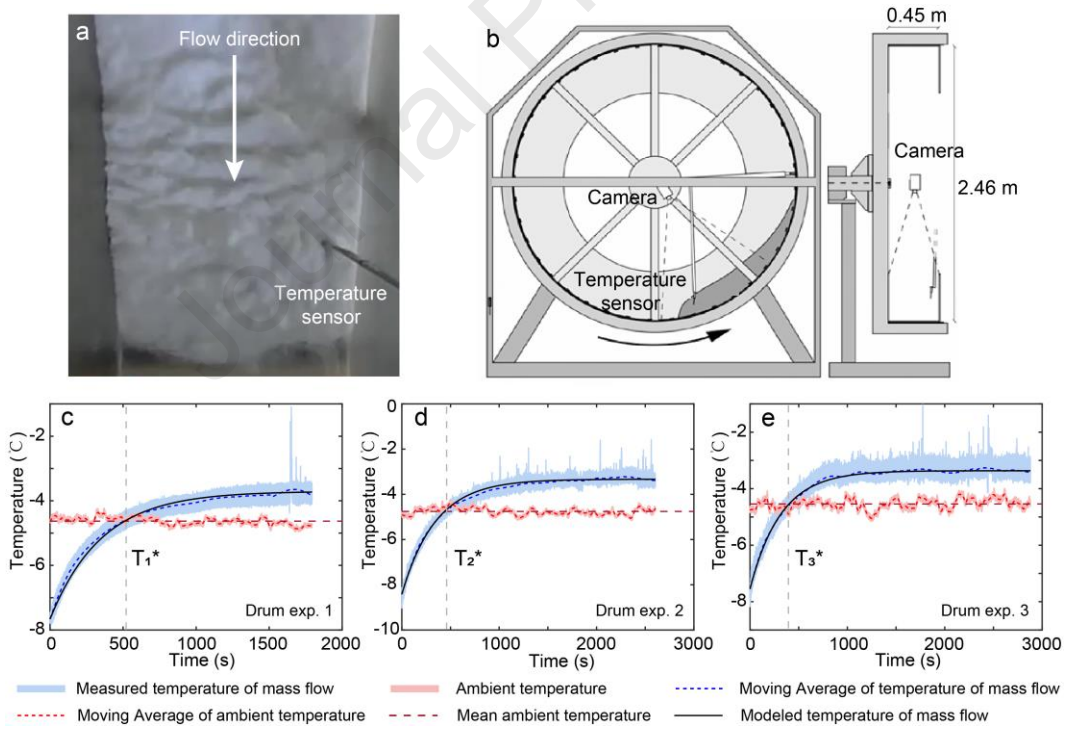

Fig. 10. Measured and simulated temperatures of ice flows in three vertically rotating drum experiments: (a) and (b) Vertically rotating drum experiment device; (c)-(e) Measured and simulated temperatures of mass flows in three experiments.

3.3 Test 3: Centrifuge modeling of a soil-ice mass flow

We conducted an experiment on a soil-ice mass flow using the HKUST 400*g*-ton centrifuge facility (https://gcf.hkust.edu.hk/) (Fig. 11a) at a centrifugal acceleration of 35*g*. In this experiment, the ice-soil mixture was released from a material box onto a horizontal bed. The released mixture had a volumetric ratio of soil to ice of 7:3, and the bed material was sand. Fig. 11b and c shows the geometric dimensions of the horizontal channel, which measures 36 cm in length and 10 cm in width, with a dry sand thickness of 10 cm. A temperature sensor (i.e. thermocouple sensor) was positioned on the surface of the channel material, centrally within the bed channel, to monitor temperature changes. We utilized a high-speed camera to capture the flow depth of the ice-soil mixture, measuring approximately 0.15 cm, and its velocity, recorded at 11 m/s, before it entered the horizontal channel (i.e. yellow part in Fig. 11b). We recorded the distribution thickness of the deposited materials in the channel after the experiment, as well as the bed temperature changes before and after the ice-soil mixture flows through the channel bed. The red line in Fig. 11c depicts the ice-soil deposition thickness along the bed channel, while the green line in Fig. 11d shows the temperature variations recorded by the sensor before and after the runout of the flow mass.

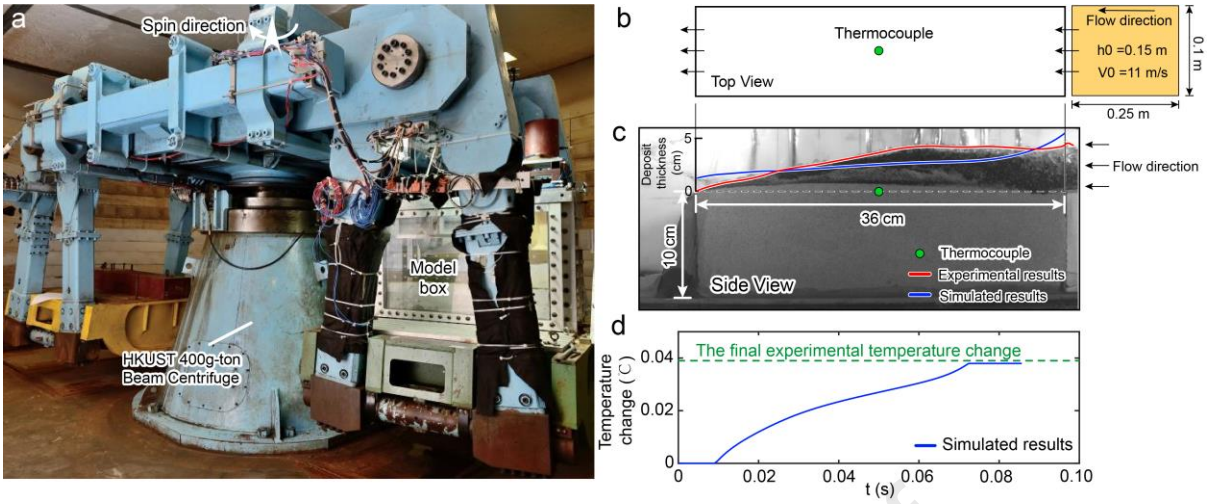

Fig. 11. Centrifuge modeling of a soil-ice mass flow and simulation analysis using the proposed model: (a) HKUST 400*g*-ton centrifuge facility, (b) Top view of the calculation domain, (c) Experimental and simulated deposit thickness, and (d) Simulated and measured temperature at the thermocouple point.

We established a numerical model that mirrors the experimental channel to validate the simulated deposition distribution and temperature changes following a soil-ice mass flow. Fig. 11b and c shows the analysis domain and the initial conditions. In the calculation domain, the left and right boundaries are defined as open boundaries, allowing for unrestricted flow conditions. On the other hand, the upper and lower boundaries are set as closed and frictionless boundaries, and no flow interactions occur across these boundaries (Fig. 11b). The initial flow depth and velocity are 0.15 m and 11 m/s, respectively. The specific heat capacities of soil and ice were 2000 and 2200 J/(kg °C), respectively. In Fig. 11c, the blue curve represents the simulated deposition, showing that the sediment accumulation thickness decreases from the inlet to the outlet (right to left). The distribution characteristics and thickness closely match the experimental results (red line). In Fig. 11d, the blue curve records the simulated temperature changes at the temperature monitoring point (Fig. 11b). The green line represents the final temperature change at this location before and after the ice-soil mixture flows through. Due to the high velocity of movement along the 36 cm horizontal channel (Fig. 11c), the duration in this section was very short. Consequently, the temperature sensors only captured the temperature changes before and after passing the monitoring point, rather than the temporal sequence of temperature changes. The simulated final temperature changes at the temperature monitoring point, before and after the experiment are very close to the experimental results.

4 Field applications

4.1 Zelunglung cascading landslide hazards on 10 September 2020

To further test the proposed model, we apply our model to analyze the Zelunglung (ZLL) rock-ice hazard chain in 2020 (Peng et al., 2022; Wang et al., 2023). The ZLL catchment (29°36′32″N, 94°58′13″E) is situated at the north side of Namcha Barwa Peak (7782 m a.s.l., Fig. 12a) in southeast Tibet. The catchment outlet is near the Yarlung Tsangpo River. Zhibai Bridge is located at the outlet, which is prone to impact by rock-ice mass flows (Fig. 12d). Based on our field investigations and soil sample analyses (Peng et al., 2022; Wang et al., 2023), we conducted multi-parameter combination simulation analyses. Several scenarios are designed for parameter sensitivity analysis, examining the effects of initial ice content, initial ice temperature, and initial solid volumetric ratio.

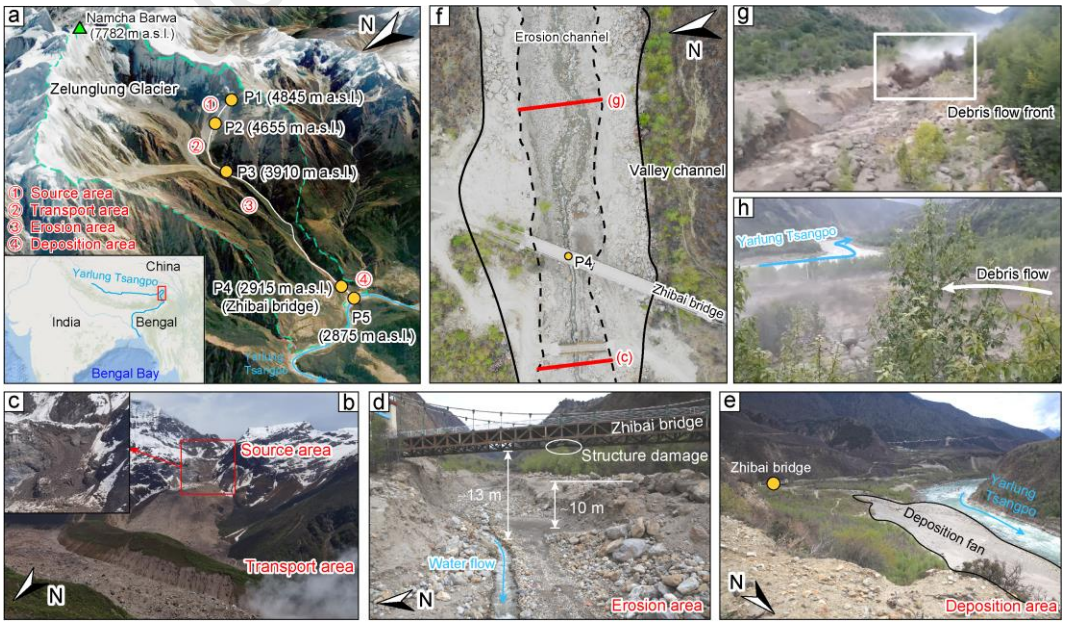

Fig. 12. The research area of ZLL cascading hazards on 10 September 2020: (a) ZLL catchment including source area, transport area, erosion area and deposition area; (b) and (c) Photos of the source area (29°36′ 26″N, 95°00′ 36″E); (d) Erosion area at P4 (Zhibai bridge) (29°36′25″N, 94°56′11″E); (e) Deposition area (29°36′25″N, 94°56′11″E); (f) Drone aerial photo at P4 (credit: Limin Zhang (corresponding author)); (g) and (h) In situ photos taken by local villagers.

Previous investigations have revealed that an initial slide, which triggered the mass flow event, involved a substantial volume of 1.16 million m^3 of rock-ice mixtures (Peng et al., 2022). The initial landslide subsequently transformed into a rock-ice avalanche. As the avalanche progressed, it entrained a substantial volume of saturated bed materials and caused the formation of a debris flow. The rapid mass flow runs for a substantial distance, reaching 9.8 km, consequently causing partial obstruction of the river course of the Yarlung Tsangpo River. In-situ photos show that the landslide-initiating deposit was found to contain ice (Fig. 12b and c). The solid materials transported by the flow subsequently deposited and resulted in the formation of a deposition fan at the outlet (Fig. 12e). Field investigations have indicated that the deposition fan has a maximum thickness of 11.4 m (Wang et al., 2023). Fig. 13 shows the recorded monthly temperatures at Nyingchi meteorological station (29.57°N, 94.47°E, 3001 m a.s.l.; 51 km to ZLL catchment), and the discharge of Yarlung Tsangpo River was about 4000 m/s^3. The mean maximum and minimum temperatures observed between August 15 and September 14, 2020, prior to the event were 27 °C and 13 °C, respectively. Daily precipitation during this timeframe fluctuated between 0 mm and 17.5 mm per day (Wang et al., 2023).

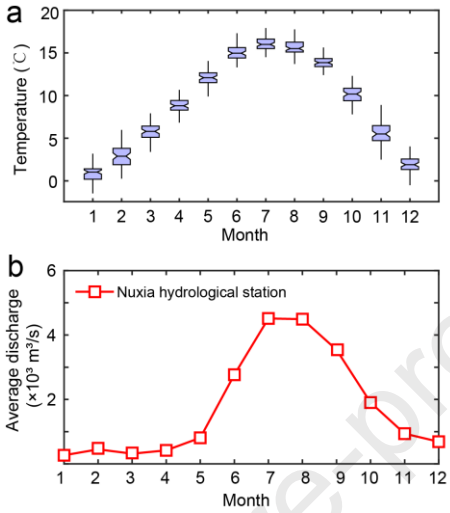

Fig. 13. (a) Monthly air temperature in the research area (Data sources: https://www.ncei.noaa.gov/); and (b) The long period monthly average runoff at the Nuxia Hydrological Station (Data source: Chen et al., 2020).

4.2 Model input and parameterization

High-resolution stereo satellite images from the ZY-3 satellite, with a spatial resolution of 2.5 m, were captured both before (5 December 2019) and after (16 December 2020) the hazard event. The satellite images were utilized to generate ground elevation maps and assess the debris depth in the source area (details see Peng et al., 2022). This study utilizes the quadratic model (Eqs. (21)-(25)) in the flow resistance analysis to consider the effects of the volumetric ratio of solid mass on the characteristics of mass flow. Table 2 provides the input parameters of the quadratic model. A grid cell size of 6 m is chosen to strike a balance between calculation accuracy and computational efficiency. The densities of rock/soil mass (ρ_r), ice (ρ_i) and water (ρ_w) are set as 2650 kg/m^3, 910 kg/m^3, and 1000 kg/m^3, respectively. Specific heat capacity values of rock/soil mass (C_r), ice (C_i) and water (C_w) are taken as 890 J/(kg °C), 2100 J/(kg °C), and 4200 J/(kg °C), respectively (Table 3). The calculation domain is divided into five zones (Fig. 14), in which superficial materials are assigned with various model parameters (Table 4). K_e and C_{dep} represent the erosion and deposition coefficients in Eq. (17), respectively, which are determined based on field surveys and empirical formulas (Chang et al., 2011; Wang et al., 2023). Heat transfer coefficients are summarized in Tables 5 and 6. Multiple simulation scenarios (Table 7) are conducted with varying initial volumetric ice contents (C_{vi0}), initial volumetric rock/soil contents (C_{vs0}), and initial solid temperatures (T_0). During the simulation, the ambient temperature is established using the temperature of the Nyingchi meteorological station (3001 m a.s.l.) as a reference (Fig. 10), and a temperature drop of 0.6 °C is applied for every 100 m of altitude increase.

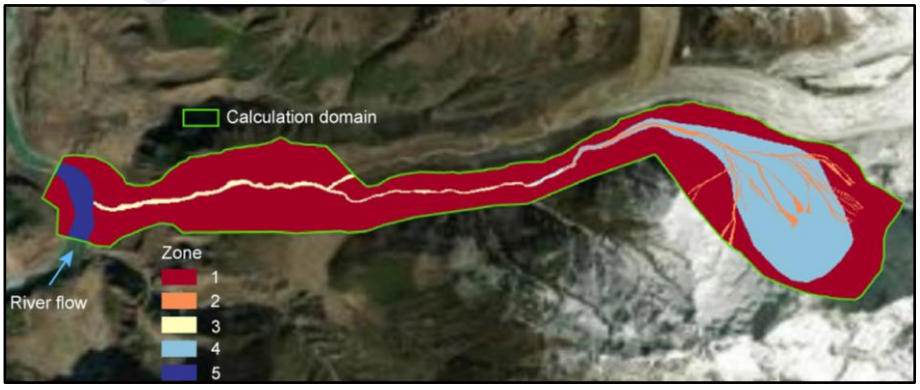

Fig. 14. Calculation domain and material zones.

Table 2. Rheological model properties and fluctuation energy parameters.

α_1	β_1	α_2	β_2	K	n_m	α_E	β_E	R_0 (kJ)
3.8	3.51	0.02	2.97	2500	0.1	0.06	1	10

Note: α_1, α_2, β_1 and β_2 are empirical parameters in Eqs. (23) and (24); K is the laminar flow resistance in Eq. (21); n_m is the manning coefficient; 1- α_E and β_E are the heat production by friction shearing and decay of fluctuation energy, respectively; R_0 is the activation energy (Eqs. (14) and (16)) (Bartelt et a., 2012).

Table 3. Mass density and specific heat capacity.

ρ_r (kg/m^3)	ρ_i (kg/m^3)	ρ_w (kg/m^3)	C_r (J/(kg °C))	C_i (J/(kg °C))	C_w (J/(kg °C))
2650	910	1000	890	2100	4200

Note: ρ_r, ρ_i, and ρ_w are the densities of rock/soil particles, ice particles, and water, respectively; C_r, C_i, and C_w are the specific heat capacities of rock/soil particles, ice particles, and water, respectively.

Table 4. Model parameters of superficial materials in five zones.

Zone ID	c_{bed} (kPa)	ϕ (°)	C_{vs*}	C_{vi*}	K_e	C_{dep}
Zone 1	30	30	0.65	0	1×10^{-6}	0.005
Zone 2	50	15	0.50	0	1×10^{-3}	0.005
Zone 3	20	15	0.55	0	5×10^{-3}	0.005
Zone 4	12	15	0.40	0.2	3×10^{-4}	0.005
Zone 5	0.1	36	0.65	0	1×10^{-6}	0.005

Note: c_{bed} and ϕ are the effective cohesion and friction angle of the bed material, respectively; C_{vs*} and C_{vi*} are the volume fractions of rock/soil and ice in the entrained materials along the erodible bed, respectively; K_e and C_{dep} are the erosion and deposition coefficients, respectively.

Table 5. Heat transfer coefficients with ambient environment.

k_{r_amb} (J/(m^2 s °C))	k_{i_amb} (J/(m^2 s °C))	k_{w_amb} (J/(m^2 s °C))
200	250	1000

Note: k_{r_amb}, k_{i_amb}, and k_{w_amb} are the heat transfer coefficients of rock/soil, ice and water with ambient environment, respectively.

Table 6. Heat transfer coefficients for rock/soil, ice and water.

k_{s_i} (J/(m^2 s °C))	k_{r_w} (J/(m^2 s °C))	k_{i_w} (J/(m^2 s °C))
200	200	200

Note: $k_{j,k}$ (j,k = s, w, i) is the heat transfer coefficient between the jth phase and kth phase.

Table 7. Simulation scenarios.

Scenario No.	C_{vs0}	C_{vi0}	T_0
1	0.2	0.4	0
2	0.2	0.4	-2
3	0.2	0.4	-4
4	0.1	0.5	0
5	0.1	0.5	-2
6	0.1	0.5	-4
7	0.2	0.5	0
8	0.2	0.5	-2
9	0.2	0.5	-4

Note: C_{vs0} and C_{vi0} are the initial volume ratios of soil and ice in the flowing mixture, respectively; T_0 is the initial temperature of the flowing mass.

4.3 Modeling results

4.3.1 Mobility of mass flow

The simulation results from Scenario 1 in Table 7 are taken as an example to showcase the simulated outcomes of flow velocity and flow depth. Figs. 15 and 16 show typical flow velocity and flow depth contours at different snapshots. The flow velocity is higher while the flow depth is lower in steep slope sections (P1-P2). As the flowing mass enters the valley channel, the flow depth increases, and the flow velocity decreases due to the gentler slope of the channel (P3-P5).

We utilized the observation results near Zhibai Bridge (P4) as a reference to validate the simulated flow velocity and flow depth. Fig. 12f shows an aerial photo of Zhibai Bridge after the hazard. Field investigations and two on-site photos indicate that at location P4, the flow depth of the mass flow was approximately 10 to 13 m (Fig. 12d). The flow velocity at this location was measured to be around 12 m/s (Peng et al., 2022).

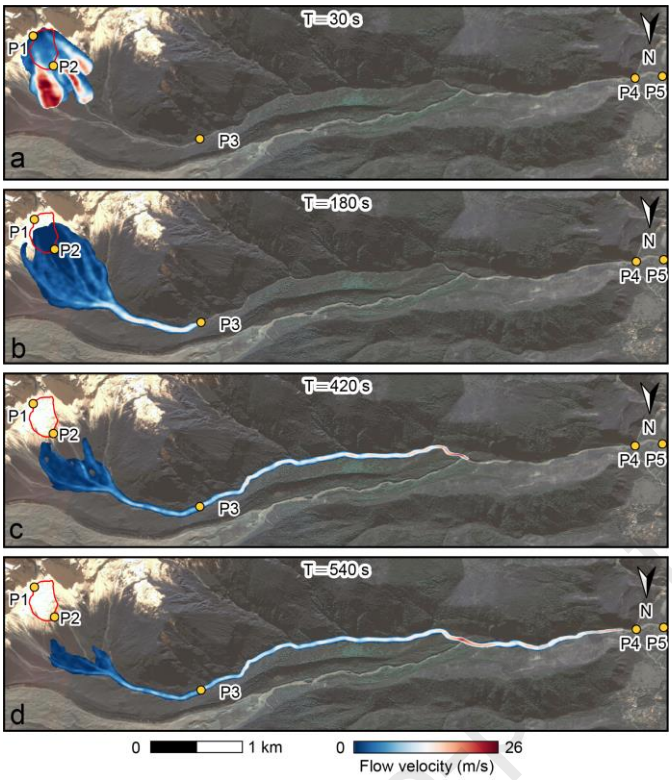

Fig. 15. Simulated flow velocity in scenario No. 1.

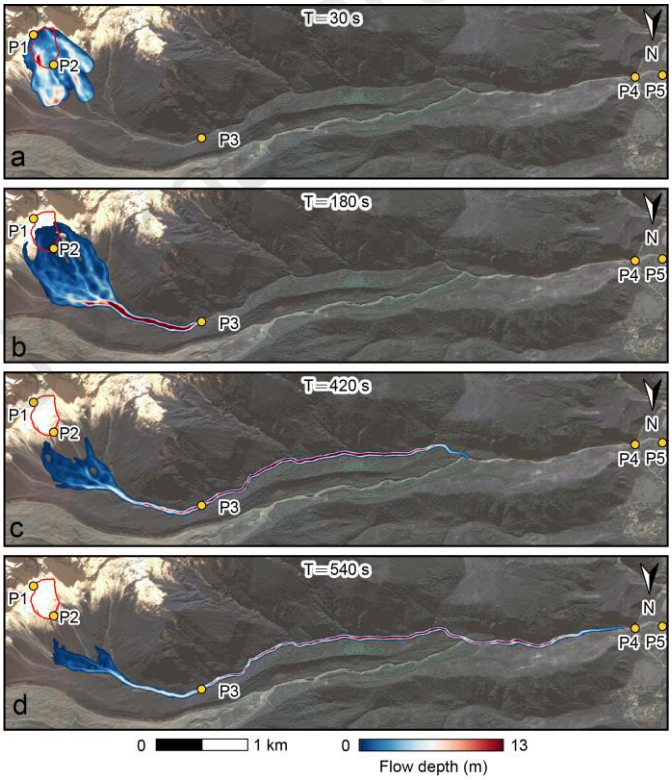

Fig. 16. Simulated flow depth in scenario No. 1.

Multi-scenario simulation results at P4 are presented in Fig. 17. For the simulated results indicated by the blue and red curves in Fig. 17, the initial solid contents are $C_{v0} = C_{vi0} + C_{vs0} = 0.6$. For the simulated results indicated by the green curves, the initial solid contents, C_v, are 0.7. According to Eqs. (22)-(24), a larger C_v value can result in a larger Manning coefficient (Eq. (22)), increased yield stress (Eq. (23)), and greater dynamic viscosity (Eq. (24)) for the flowing mass. Consequently, a larger C_v value causes larger resistance for the flow mass, and the simulated flowing mass represented by the green curves will reach point P4 later compared with those indicated by the blue/red curves. Despite variations in the arrival time, the simulated flow velocity and flow depth at Zhibai Bridge consistently agree with the observed results. We also compare the difference in the flow velocity with and without fluctuation energy to verify the enhanced effect of fluctuation energy on flow velocity. Fig. 18 shows that neglecting fluctuation energy will result in an underestimation of the average flow velocity.

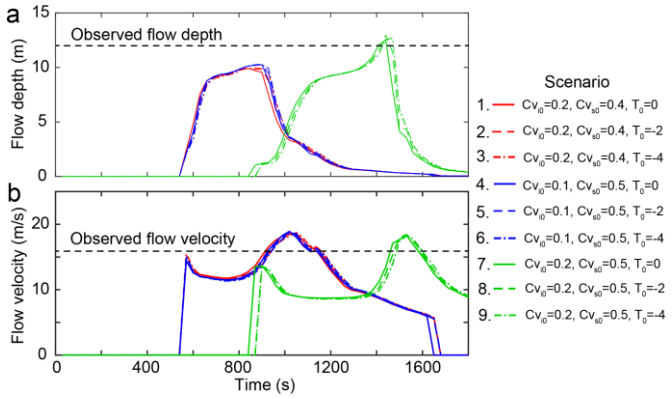

Fig. 17. Simulated and observed flow velocity and flow depth at Zhibai Bridge (P4).

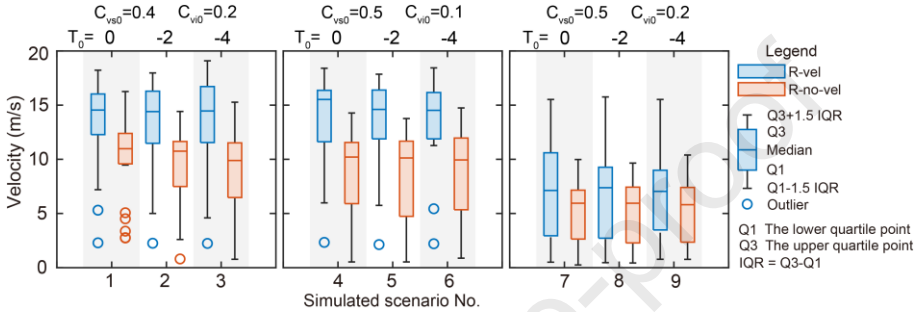

Fig. 18. Variations of flow velocity with initial temperature (T_0), initial volumetric debris ratio (C_{vs0}) and ice ratio (C_{vi0}), accounting for enhanced mobility due to fluctuation energy (R-vel) and disregarding enhanced mobility resulting from fluctuation energy (R-no-vel) under different scenarios.

4.3.2 Amplification of mass flow volume

Figs. 12e and 19b demonstrate the final distribution of erosion and deposition depth in the simulation. The simulated erosion mainly occurs within the P3-P5 section, with erosion depth ranging from 1 m to 5 m, and an entrained mass volume of approximately $(4.95 \pm 0.11) \times 10^5$ m^3 (Fig. 20b). The entrainment ratio (*ER*), i.e. the ratio of the volume of the entrained mass to the volume of source materials, is 0.44, which is relatively small among historical cases (*ER* = 1-9) (Hungr and Evans, 2004; Peng et al., 2022), such as the 2000 Yigong landslide with *ER* = 9. It is because the flow channel is relatively narrow, and the thickness of erodible bed geo-materials is rather small (Peng et al., 2022). As the mass flow progresses towards the gully outlet, the deposition process becomes dominant due to the gradual decrease in terrain slope. Simultaneously, influenced by the river flow of the Yarlung Tsangpo River, a deposition fan with a maximum thickness of approximately 10 m was formed.

4.3.3 Hazard propagation and transformation

Fig. 20 further demonstrates the simulated propagation process and the evolution of hazard types on the September 10, 2020, Zelunglung hazard chain. Section P1-P2 is characterized by the highest average slope, section P3-P5 the lowest slope, and section P2-P3 a moderate slope (Fig. 20b). Fig. 20c illustrates that the erosion zone is situated at P3-P4. In Fig. 20c, the green point indicates the field observation location with an erosion depth of 3 m. The simulated results closely match the in-situ observations. The whole hazard chain process consists of rock-ice avalanche (P1-P2), viscous debris flow (P2-P3), diluted debris-ice flow (P3-P4) and debris flood (P4-P5) (Fig. 20d). Simulated results show that the initial temperature has negligible impacts on the flow dynamic process (Figs. 20d-20e). In Section P1-P2, the detached geo-materials undergo an acceleration process (Fig. 20e) and a minor portion of the solid mass within this section experiences deposition on the slope surface (Fig. 20d). In the transportation area (P2-P3), the deposition rate of solid materials is slow. The flow velocity exhibits an initial surge, reaching its peak, and subsequently undergoes a gradual decline (Fig. 20d). The simulated results show that the hazard mass has undergone a series of transformations, from an avalanche to a subsequent stage of debris flow, and eventually evolving into a debris flood (Fig. 20d). The validity of this analysis result has been confirmed through field investigations and the examination of on-site video (Fig. 12).

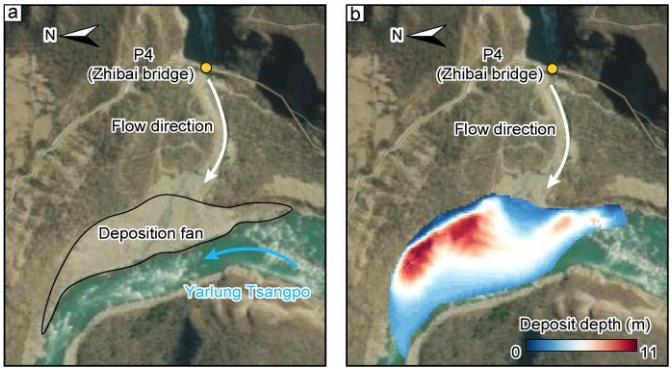

Fig. 19. (a) Deposition fan in the 10 September 2020 rock-ice hazard, and (b) Simulated deposition thickness.

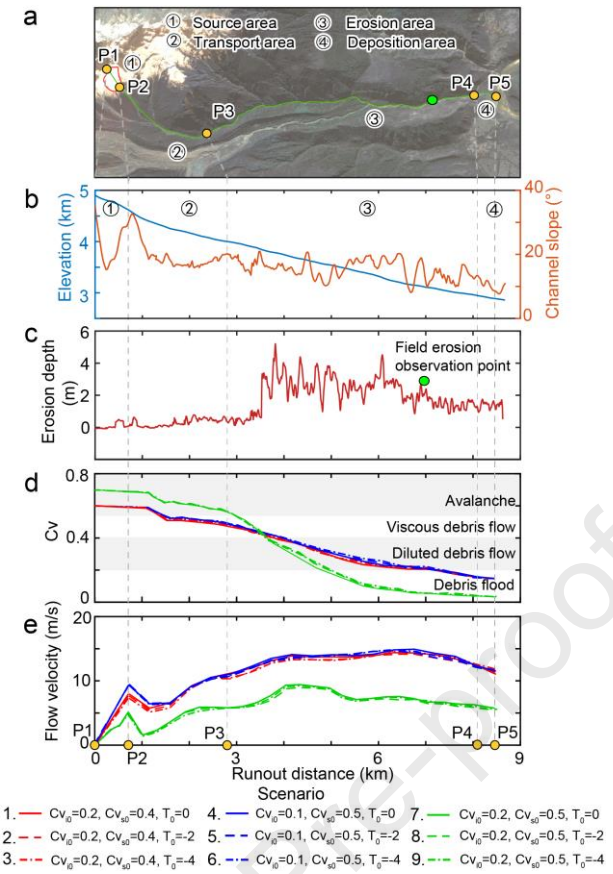

Fig. 20. (a) ZLL catchment, (b) Ground elevation and catchment channel slope, (c) Erosion depth along P1-P5, (d) Multi-hazard transformation over time reflected by evolution of volumetric solid concentration (C_v), and (e) Flow velocity along P1-P5.

4.3.4 Energy evolution and ice-water phase change

Fig. 21 illustrates the energy evolution of the generated mass flow throughout the propagation process, alongside the evolution of volumetric ice content. This analysis encompasses cumulative friction work, kinetic energy, fluctuation energy (e.g. random kinetic energy), and internal energy.

The energy characteristics of the flowing mass vary as it moves to different locations. During the initial stage of motion (P1-P3), characterized by high solid volume contents (Fig. 20d and e), the debris flow carries a substantial amount of kinetic energy (Fig. 21c). The fluctuation energy in P2-P3 is much higher than other stages, indicating the relatively intense collision of solid particles within the mass flow when moving along the steep slope (Fig. 20b). Meanwhile, the internal energy of the mass flow witnesses a gradual increasing trend (Fig. 21c). Subsequently, despite a relatively constant movement velocity, the kinetic energy of the mass flow gradually diminishes and stabilizes as the solid volume ratio decreases. As the movement progresses, the frictional energy gradually increases (Fig. 21b). Concurrently, the internal energy of the geo-material within the mass flow steadily increases (Fig. 21e), resulting in gradual ice melting (Fig. 21f).

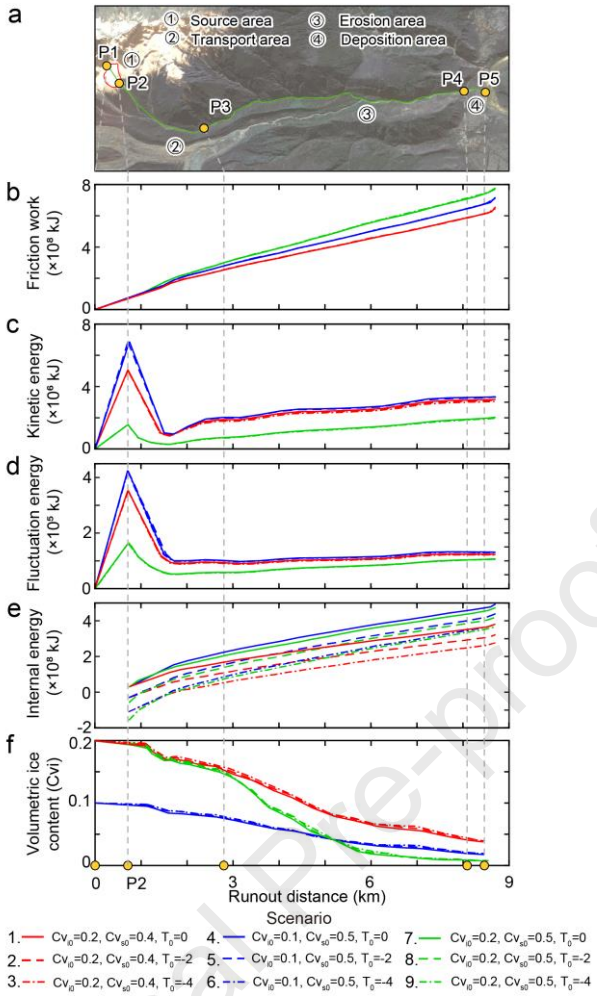

Fig. 21. Simulated spatiotemporal evolution of the Zelunglung hazard chain: (a) ZLL catchment, (b) Total friction work, (c) Total kinetic energy, (d) Total fluctuation energy, (e) Total internal energy, and (f) The evolution of volumetric ice concentration along P1-P5.

The simulation results indicate that, during the movement process, the kinetic energy associated with translational velocity significantly exceeds the fluctuation kinetic energy arising from the chaotic motion of solid particles (Fig. 21c and d). Furthermore, we found that the initial solid temperature has little impact on the kinetic energy. In contrast, varying the initial solid volumetric ratio leads to differences in the kinetic energy during the propagation process.

Variations in energy evolution led to differences in ice content evolution. It is noteworthy that during the initial stages of motion, the reduction in ice volume content occurs slowly, accompanied by substantial velocity variations in the mass flow. This observation suggests that, in this phase, external influences predominantly impact the kinetic energy of the mass flow (Fig. 21c). Subsequently, as the velocity stabilizes, the external energy input primarily facilitates the melting of ice (Fig. 21f). Fig. 21f further shows that under the same initial material composition ratio, differences in initial solid temperature result in minimal variations in corresponding ice content changes. In contrast, differences in the initial solid material composition lead to significant variations in the ice content evolution during the movement process, which is reflected by the curves of different colors in Fig. 21f.

The case study of the Zelunglung hazard in 2020 also highlights the effects of erosion-entrainment-deposition, ice-water phase change, and multi-hazard transformation on the dynamics and mobility of glacier cascading hazards. Erosion-entrainment significantly increases the volume of the flowing mass ($(4.95 \pm 0.11) \times 10^5$ m³ in this study), resulting in the enhanced transport of geo-materials to valley outlets and river channels. In addition, the processes of erosion-entrainment-deposition and ice-water phase transitions lead to changes in solid components and the occurrence of multi-hazard transformations. These changes affect solid energy fluctuation (Eqs. (14) and (16)) and flow resistance (Eq. (21)), thereby altering the mobility and dynamics of the mass flow (Figs. 18, 20, and 21).

5 Discussion

A typical glacier landslide hazard chain involves the evolution of physical properties of the mass flow through erosion and entrainment, transformation of hazard types, ice-water phase changes, and enhanced mobility. Table 8 summarizes existing computational tools for simulating the propagation of mass flows, indicating that the existing models are limited in their ability to analyze multi-hazard processes, energy evolution, and ice-water phase changes.

This paper presents an integrated numerical model GMFA (Glacier Mass Flow Analysis) to help solve these problems. The proposed model is capable of simulating mass flows with varying volumetric contents of soil, ice, and water, including avalanches, debris flows, and debris floods. Firstly, we take volumetric solid content (C_v) to distinguish different hazard types. Eqs. (2) and (3) are taken to update the volumetric solid content during the propagation process. Secondly, we introduced three independent equations to separately analyze the internal energy evolution of ice, soil, and water within the flowing mass (Eqs. (11)-(13)), thereby achieving a physical solution for ice-melting water. Entrainment-deposition and ice-water phase changes, two factors that significantly affect the composition ratios of different materials within the flowing mass, have been considered. Thirdly, as the solid volumetric content (C_v) changes during motion, the physical properties and the resistance of the flowing mass will inevitably change, which are quantified using the quadratic model (Eq. (21)). In Eq. (21), the frictional and viscous behavior, turbulent effects, and resistance arising from solid-particle contacts within the flowing mass are considered. Eq. (22) is taken to calculate the equivalent Manning coefficient of the flowing mass. Eqs. (23) and (25) are employed to calculate the yield stress of flowing mass with different values of C_v. Eq. (24) is used to obtain the

dynamic viscosity. Benchmark tests have been conducted to validate the proposed model considering multiple parameter combinations. By comparing the simulated results with field observations, the proposed model is validated as an accurate tool for analyzing real-world field problems.

On the other hand, while the proposed model effectively simulates the propagation of mass flows, it does not address the initiation and stability issues of frozen slopes. The GMFA model simplifies computational analysis using a depth-averaged approach, which is highly efficient and enables large-scale analysis. This approach is commonly used to simplify the complex dynamics of flowing solid-water mixtures by averaging physical properties over the flow depth, which has been verified and used in previous studies (FLO-2D, 2009; Chen et al., 2015; Sansone et al., 2021; Xia et al., 2023). When the flow depth (e.g. 10^{-1}-10^{1} m) is much smaller than the runout distance (e.g. 10^{3}-10^{5} m), the depth-averaged method can accurately capture flow characteristics, such as flow depth and velocity (Sansone et al,.2021; Xia et al., 2023). However, there are still some limitations. Firstly, the depth-average method does not capture vertical variations in velocity and concentration. Secondly, such method may struggle to represent the effects of large particles or debris (radius > 1m), which can influence the movement of solid-water mixtures. In addition, the momentum exchange between the fluid and particles, as well as the phase segregation within the flowing mass, are not considered in this depth-averaged simulation model. Particle segregation, with a solid-dominated front and fluid-dominated back, can be simulated using multi-phase mass flow models (such as r.avaflow in Table 8). Multi-phase flow simulation methods can capture the physical processes necessary for analyzing the impacts of hazard chains involving interactions between solid and fluid phases. These advanced methods require governing equations for the mass and momentum conservation of different phases.

Table 8. Summary of mass flow simulation models.

Model	Ice-water phase change?	Energy equation?	Multi-hazard cascading process?	Multi-phase flow?	Depth-average method?	Source
GMFA	Yes	Yes	Yes	No	Yes	This study
FLO-2D	No	No	Yes	No	Yes	O'Brien et al. (1993)
DAN	No	No	No	No	Yes	Hungr (1995)
DMM	No	No	No	No	Yes	Kwan and Sun (2006)
Debris2D	No	No	No	No	Yes	Liu and Huang (2006)
FLATModel	No	No	No	No	Yes	Medina et al. (2008)
MassMov2D	No	No	No	No	Yes	BeguerPiia et al. (2009)
DAN3D	No	No	No	No	Yes	Hungr and McDougall (2009)
RAMMS	No	No	No	No	Yes	Batelt et al. (2013)
EDDA 1.0	No	No	Yes	No	Yes	Chen et al. (2015)
EDDA 2.0	No	No	Yes	No	Yes	Shen et al. (2018)
Flow-R	No	No	No	No	No	Horton et al. (2013)
TITAN2D	No	No	No	No	Yes	Titan2D (2007)
Kanako 2D	No	No	No	No	Yes	Nakatani et al. (2008)
TOCHNOG	No	No	No	No	No	Crosta et al. (2003)
Massflow	No	No	Yes	Yes	Yes	Ouyang et al. (2013)
r.avaflow	Yes	No	Yes	Yes	Yes	Mergili et al. (2017)

6 Conclusions

This paper presents a new depth-integrated numerical model, GMFA (glacier mass flow analysis), for analyzing the propagation process of glacier landslide cascading hazards. The proposed model is distinguished by: (1) incorporating depth-averaged fluctuation energy and internal energy, (2) integrating the ice-water phase change and the entrainment-deposition process, and (3) accounting for the corresponding effects on the runout characteristics of the mass flow. These distinctive features make this model capable of analyzing volume amplification, ice-water phase changes, and multi-hazard transformations within the glacier hazard chain process. The model is a powerful tool for regional risk assessment of glacier cascading hazards under climate change. The main conclusions are summarized as follows:

(1) For glacier cascading hazards, the flowing mass consists of ice, water, and soil/rock. Variations in the mass concentration of each phase can result in different flow features throughout the whole propagation process. As the solid concentration changes, the flow mass can encompass various hazard types, including an avalanche, a viscous debris flow, a diluted debris flow and a debris flood. Consequently, the mechanical properties of the flowing mass undergo changes, e.g. rheological properties, which subsequently result in the spatiotemporal evolution of the dynamic characteristics of the flowing mass. These variations are attributed to the ice-water phase change and erosion/entrainment-deposition processes.

(2) Multi-physics coupled governing equations are proposed to delineate the physical process of glacier mass flow propagation. Eqs. (2) and (3) are taken to update the volumetric soil and ice content, and volumetric solid content (C_v) is employed to distinguish different hazard types. Three equations (Eqs. (11)-(13)) are employed to separately analyze the internal energy evolution of ice, soil, and water within the flowing mass, thereby solving for the ice-melting amount. Furthermore, mass exchange in the runout channel (Eq. (17)) is integrated into the mass and momentum conservation equations (Eqs. (1)-(5)). An explicit finite volume method is employed to solve the governing equations, which enables the new model to rapidly simulate the propagation process of large-scale glacier landslide hazard chains.

(3) Three numerical tests have been conducted to verify the proposed model. In Test 1, a 2D dam-breaching flow problem is solved to validate the performance in simulating the flowing process. Test 2 is conducted to verify the evolution of ice internal energy in three rotating drum experiments, where the flowing velocity and shearing forces were controlled. In Test 3, the deposition distribution and temperature variations are analyzed in the movement of a soil-ice mass flow in a centrifuge experiment, to verify flow dynamics and energy equations.

(4) The model is applied to simulate a large-scale rock-ice hazard chain in Southeastern Tibet to test the performance of the model in catchment-scale analysis. The multi-scenario simulation results indicate an entrained mass volume of $(4.95 \pm 0.11) \times 10^5$ m^3, with a ratio of entrained mass volume to source material volume at 0.44. As the runout distance extends, solid concentration decreases from 0.6-0.7 to 0.1-0.15, indicating a transition from an avalanche to a debris flood. The internal energy of the flowing mass increases and causes rapid ice melting from ice contents of 0.1-0.2 to almost 0. The simulated results demonstrate a typical multi-hazard transformation process, characterized by an amplification of volume and ice-water phase change of the flowing mass, which agrees well with field observations. The processes of erosion-entrainment-deposition and ice-water phase transitions led to changes in solid components and the occurrence of multi-hazard transformations during dynamic processes.

Declaration of competing interest

The authors declare that they have no known competing financial interests or personal relationships that could have appeared to influence the work reported in this paper.

Acknowledgments

This work obtained supports from the National Natural Science Foundation of China (Grant No. U20A20112), and the Research Grants Council of the Hong Kong SAR Government of China (Grant Nos. T22-606/23-R and 16206923).

References

Bartelt, P., Buser, O., Platzer, K., 2006. Fluctuation-dissipation relations for granular snow avalanches. J. Glacial. 52, 631–643.

Bartelt, P., Bühler, Y., Buser, O., Christen, M., Meier, L., 2012. Modeling mass-dependent flow regime transitions to predict the stopping and depositional behavior of snow avalanches. J. Geophys. Res., 117(F1), F01015.

Buser, O., P. Bartelt., 2009. Production and decay of random kinetic energy in granular snow avalanches. J. Glacial. 55(189), 3–12.

Chang, D. S., Zhang, L. M., Xu, Y., Huang, R. Q., 2011. Field testing of erodibility of two landslide dams triggered by the 12 May Wenchuan earthquake. Landslides 8, 321–332.

Chen, C., Zhang, L. M., Xiao, T., He, J., 2020. Barrier lake bursting and flood routing in the Yarlung Tsangpo Grand Canyon in October 2018. J. Hydrol. 583, 124603.

Chen, H. X., Zhang, L. M., 2015. EDDA 1.0: integrated simulation of debris flow erosion, deposition and property changes. Geosci. Model. Dev. 8, 829–844.

Crosta, G. B., Imposimato, S., Roddeman, D. G., 2003. Numerical modelling of large landslides stability and runout, Nat. Hazards Earth Syst. Sci. 3, 523–538.

Delaney, K. B., Evans, S. G., 2015. The 2000 Yigong landslide (Tibetan Plateau), rockslide-dammed lake and outburst flood: Review, remote sensing analysis, and process modelling. Geomorphology 246, 377–393.

Egashira, S., Honda, N., Itoh, T., 2001. Experimental study on the entrainment of bed material into debris flow. Phys. Chem. Earth Pt. C, 26, 645–650.

Evans, S. G., Delaney, K. B., 2015. Catastrophic mass flows in the mountain glacial environment, Snow and ice-related hazards, risks and disasters. Elsevier 563–606.

Feng, Z. T., Fan, X. M., Ni, T., Deng, Y., Zou, C. B., Zhang, J., Xu, Q., 2023. How ice particles increase mobility of rock-ice avalanches: insights from chute flows simulation of granular rock-ice mixtures by discrete element method. J. Geophys. Res-Earth. 128, e2023JF007115.

Fennema, R. J., Hanif Chaudhry, M., 1987. Simulation of one-dimensional dam-break flows. J. Hydraul. Res. 25(1), 41–51.

FLO-2D Software Inc. FLO-2D reference manual, Nutrioso, Arizona, USA, 2009.

Fraccarollo, L., Papa, M., 2000. Numerical simulation of real debris flow events, Phys. Chem. Earth Pt. B, 25, 757–763.

Goodwin, S. R., Choi, C. E., 2021. A depth-averaged SPH study on spreading mechanisms of geophysical flows in debris basins: Implications for terminal barrier design requirements. Comput. Geotech. 141, 104503.

Graf, W. H., 1984. Hydraulics of sediment transport, Water Resources Publications, Colorado.

Herschel, W. H., Bulkley, R., 1926. Konsistenzmessungen von Gummi-Benzollösungen. Kolloid-Zeitschrift, 39(4), 291–300.

Horton, P., Jaboyedoff, M., Rudaz, B., Zimmermann, M., 2013. Flow-R, a model for susceptibility mapping of debris flows and other gravitational hazards at a regional scale, Nat. Hazards Earth Syst. Sci., 13, 869–885.

Hugonnet, R., Mcnabb, R., Berthier, E., Menounos, B., Nuth, C., Girod, L., Farinotti, D., Huss, M., Dussaillant, I., Brun, F., Kääb, A., 2021. Accelerated global glacier mass loss in the early twenty-first century. Nature 592, 726–731.

Hungr, O., 1995. A model for the runout analysis of rapid flow slides, debris flows, and avalanches, Can. Geotech. J., 32, 610–623.

Iverson, R. M., Reid, M. E., Logan, M., LaHusen, R. G., Godt, J. W., Griswold, J. P., 2011. Positive feedback and momentum growth during debris-flow entrainment of wet bed sediment, Nat. Geosci., 4, 116–121.s

Iverson, R. M., 2012. Elementary theory of bed-sediment entrainment by debris flows and avalanches, J. Geophys. Res.-Earth, 117, F03006.

Jacquemart, M., Loso, M., Leopold, M., Welty, E., Berthier, E., Hansen, J. S. S., 2020. What drives large-scale glacier detachments? Insights from Flat Creek glacier, St. Elias Mountains, Alaska. Geology, 48, 703–707.

Jiang, R. C., Zhang, L. M., Peng, D. L., He, X., He, J., 2021. The landslide hazard chain in the Tapovan of the Himalayas on 7 February 2021. Geophys. Res. Lett. 48, e2021GL093723.

Jiang, T., Dai, F., Zhang, L. M., Jiang, R. C., Hong, H. Y., Wei, M. D., 2024. Simulation of collapse process of ice-rich slope: A case of 2016 Giant Aru Glacier Collapse in Tibet, China. J. Rock Mech. Geotech., https://doi.org/10.1016/j.jrmge.2024.11.022.

Julien, P. Y., Lan, Y., 1991. Rheology of hyper concentrations. J. Hydraul. Res. 117, 346–353.

Kääb, A., Leinss, S., Gilbert, A., Bühler, Y., Gascoin, S., Evans, S. G., 2018. Massive collapse of two glaciers in western Tibet in 2016 after surge-like instability. Nat. Geosci. 11, 114–120.

Kozicki, W., Chou, C. H., Tiu, C., 1966. Non-Newtonian flow in ducts of arbitrary cross-sectional shape. Chem. Eng. Sci., 21(8), 665–679.

Kozicki, W., Tiu, C., 1967. Non-Newtonian flow through open channels. Can. J. Chem. Eng., 45(3), 127–134.

Krishnappan, B. G., Lau, Y. L., 1986. Turbulence Modeling of Flood Plain Flows. J. Hydraul. Eng-ASCE. 112(4), 251.

Kwan, J. S. H., Sun, H. W., 2006. An improved landslide mobility model. Can. Geotech. J. 43(5), 531-539.

Li, X. Y., Sovilla, B., Jiang, C. F., Gaume J., 2021. Three-dimensional and real-scale modeling of flow regimes in dense snow avalanches. Landslides 18(10), 3393-3406.

Liu, K. F., Huang, M. C., 2006. Numerical simulation of debris flow with application on hazard area mapping. Computational Geoscience, 10(2), 221-240.

Millan, R., Mouginot, J., Rabatel, A., Morlighem, M., 2022 Ice velocity and thickness of the world's glaciers. Nat. Geosci. 15, 124–129.

Mani, P., Allen, S., Evans, S. G., Kargel, J. S., Mergili, M., Petrakov, D., Stoffel, M., 2023. Geomorphic process chains in high-mountain regions—A review and classification approach for natural hazards assessment. Rev. Geophys. 61, e2022RG000791.

McDougall, S., Hungr, O., 2005. Dynamic modelling of entrainment in rapid landslides, Can. Geotech. J., 42, 1437–1448.

Medina, V., Hürlimann, M., Bateman, A., 2008. Application of FLATModel, a 2-D finite volume code, to debris flows in the northeastern part of the Iberian Peninsula, Landslides, 5, 127–142.

Mergili, M., Fischer, J., Krenn, J., Pudasaini, S. P., 2017. r.avaflow v1, an advanced open-source computational framework for the propagation and interaction of two-phase mass flows. Geosci. Model Dev. 10, 553–569.

Nakatani, K., Wada, T., Satofuka, Y., Mizuyama, T., 2008. Development of "Kanako 2D (Ver.2.00)," a user-friendly one- and two-dimensional debris flow simulator equipped with a graphical user interface. International Journal of Erosion Control Engineering 1, 62–72.

O'Brien, J. S., Julien, P. Y., 1988. Laboratory analysis of mudflow properties. J. Hydraul. Res. 114, 877–887.

Ouyang, C., He, S., Xu, Q., Luo, Y., Zhang, W., 2013. A MacCormack-TVD finite difference method to simulate the mass flow in mountainous terrain with variable computational domain. Comput Geosci-UK. 52, 1-10.

Peng, D. L., Zhang, L. M., Jiang, R. C., Zhang, S., Shen, P., Lu, W., He, X., 2022. Initiation mechanisms and dynamics of a debris flow originated from debris-ice mixture slope failure in southeast Tibet, China. Eng. Geol. 307, 106783.

Pudasaini, S. P., Krautblatter, M., 2014. A two-phase mechanical model for rock-ice avalanches. J. Geophys. Res. Earth Surf. 119 (10), 2272–2290.

Pudasaini, S. P., Mergili, M., 2019. A multi-phase mass flow model. J. Geophys. Res. Earth Surf. 124, 2920–2942.

Pierson, T. C. and Scott, K. M., 1985 Downstream dilution of a lahar: transition from debris flow to hyperconcentrated streamflow, Water Resour. Res., 21, 1511–1524.

Quan Luna, B., Remaître, A., van Asch, T. W., Malet, J. P., Van Westen, C. J., 2012. Analysis of debris flow behavior with a one-dimensional run-out model incorporating entrainment, Eng. Geol. 128, 63–75.
Ren, Y. H., Yang, Q. Q., Cheng, Q. G., Cai, F., Su. M., 2021. Solid-liquid interaction caused by minor wetting in gravel-ice mixtures: a key factor for the mobility of rock-ice avalanches. Eng. Geol. 286,106072.
Sansone, S., Zugliani, D., Rosatti, G., 2021. A mathematical framework for modelling rock–ice avalanches. J. Fluid. Mech. 919.
Shen, P., Zhang, L., Chen, H., Fan, R., 2018. EDDA 2.0: integrated simulation of debris flow initiation and dynamics considering two initiation mechanisms, Geosci. Model Dev., 11, 2841–2856.
Siddique, T., Haris, P. M., Pradhan, S. P., 2022. Unraveling the geological and meteorological interplay during the 2021 Chamoli disaster, India. Natural Hazards Research, 2(2), 75-83.
Sosio, R., Crosta, G. B., Chen, J. H., Hungr, O., 2012. Modelling rock avalanche propagation onto glaciers. Quat. Sci. Rev. 47, 23–40.
Takahashi, T., Nakagawa, H., Harada, T., Yamashiki, Y., 1992. Routing debris flows with particle segregation. J. Hydraul. Res. 118, 1490–1507.
Titan2D User Guide, Release 2.0.0, 2007. Geophysical Mass Flow Group.
Toro, E. F., 2001. Shock-Capturing Methods for Free-Surface Shallow Flow. John Wiley & Sons, Ltd.
Van den Bout, B., Tang, C., van Westen, C., Jetten, V., 2022. Physically based modeling of co-seismic landslide, debris flow, and flood cascade, Nat. Hazards Earth Syst. Sci., 22, 3183–3209.
Valero, C. V., Jones, K. W., Bühler, Y., Bartelt, P., 2015. Release temperature, snow-cover entrainment and the thermal flow regime of snow avalanches. J. Glacial. 61(225), 173-184.
Velechovsky, J.; Francois, M.; Masser, T., 2019. Direction-aware slope limiter for three-dimensional cubic grids with adaptive mesh refinement. Comput. Math. Appl, 78, 670–687
Voellmy, A. 1955. Uber die Zerstorungskraft von Lawinen. Schweizerische Bauzeitung, Jahrg., 73, 159–162.
Wang, T. F., Huang, T. S., Shen, P., Peng, D. L., Zhang, L. M., 2023. The mechanisms of high mobility of a glacial debris flow using the Pudasaini-Mergili multi-phase modeling. Eng. Geol. 322, 107186.
Wei, Q., Liu, Y., Yan, Q., Yao, T., Wang, M., Huang, H., Hu, Y., 2023. The glacier-climate interaction over the Tibetan Plateau and its surroundings during the Last Glacial Maximum. Geophys. Res. Lett. 50, e2023GL103538.
Wei, M. D., Zhang, L. M., Jiang, R. C., 2024. A conceptual model for evaluating the stability of high-altitude ice-rich slopes through coupled thermo-hydro-mechanical simulation, Eng. Geol. 334, 107514.
Xu, Q., Shang, Y. J., Asch, T. V., Wang, S. T., Zhang, Z. Y., Dong, X. J., 2012. Observations from the large, rapid Yigong rock slide - debris avalanche, southeast Tibet. Can. Geotech. J. 49, 589–606.
Xu, Z, D., Zarch, M. K., Wang, H, J., Zeng, Z. X., Zhang, L. M., 2024. Responses of Ice-Soil Mixtures to Ice Melting. Can. Geotech. J. online, https://doi.org/10.1139/cgj-2024-0469.
Xia, X. L., Jarsve, K. T., Dijkstra, T., Liang, Q. H., Meng, X. M., Chen, G., 2023. An integrated hydrodynamic model for runoff-generated debris flows with novel formulation of bed erosion and deposition. Eng. Geol. 326(5), 107310.
Yin, Y. P., Li, B., Gao, Y., Wang, W. P., Zhang, S. L., Zhang, N., 2023. Geostructures, dynamics and risk mitigation of high-altitude and long-runout rockslides. J. Rock Mech. Geotech. 15(1), 66-101.
Xiao, S. H., Zhang, L. M., Xiao, T., Jiang, R. C., Peng, D. L., Lu, W. J., He, X., 2024. Landslide damming threats along the Jinsha River, China. Engineering 42, 326-339.
Zhao, B., Su, L. J, 2024. Complex spatial and size distributions of landslides in the Yarlung Tsangpo River (YTR) basin. J. Rock Mech. Geotech., https://doi.org/10.1016/j.jrmge.2024.01.021.

Dr. Limin Zhang is Chair Professor and Head of the Department of Civil and Environmental Engineering and Director of Digital Cities and Smart Hazard Mitigation Laboratory at the Hong Kong University of Science and Technology. Dr. Zhang specializes in slopes, dams, and geotechnical risk assessment and management. He is Chair of International Society of Soil Mechanics and Geotechnical Engineering (ISSMGE)'s TC210 on Embankment Dams, Past Chair of ASCE Geo-Institute's Risk Assessment and Management Committee, Editor-in-Chief of Georisk, Special Editor of *Geodata and AI*, Associate Editor of ASCE's *Journal of Geotechnical and Geoenvironmental Engineering*, and editorial board member of *Engineering Geology*, *Computers and Geotechnics* and other journals. He is recipient of the Chinese National Engineer Award, ASCE Ralph Peck Award, ISSMGE's Lacasse Lecture Award and GEOSNet's Wilson Tang Lecture Award.

Dr. Ruochen Jiang obtained his PhD in 2024 from the Hong Kong University of Science and Technology (HKUST) and currently works as the Post-doctoral Research Fellow at HKUST. His research interests include (i) remote sensing analysis of glacier hazards, (ii) modelling and prediction of climate-driven valley glacier dynamics, and (iii) modelling of glacier landslide hazard chains. He has published several research papers in esteemed journals such as *Engineering, Geophysical Research Letter, and Engineering Geology.*

Declaration of interests

☒ The authors declare that they have no known competing financial interests or personal relationships that could have appeared to influence the work reported in this paper.

☐The authors declare the following financial interests/personal relationships which may be considered as potential competing interests:

River Damming Threats by Climate-Driven Glacier Detachments

Ruochen Jiang[1]; Limin Zhang, Ph.D., F.ASCE[2]; and Wenjun Lu, Ph.D.[3]

[1]Dept. of Civil and Environmental Engineering, Hong Kong Univ. of Science and Technology, Hong Kong, China; HKUST Shenzhen Research Institute, Shenzhen, China.
Email: rjiangad@connect.ust.hk
[2]Dept. of Civil and Environmental Engineering, Hong Kong Univ. of Science and Technology, Hong Kong, China; HKUST Shenzhen-Hong Kong Collaborative Innovation Research Institute, Futian, Shenzhen, China. Email: cezhangl@ust.hk
[3]Dept. of Civil and Environmental Engineering, Hong Kong Univ. of Science and Technology, Hong Kong, China. Email: wenjunlu@ust.hk

ABSTRACT

Yarlung Tsangpo on the Tibetan Plateau is the highest large river in the world. Valley glaciers in the Yarlung Tsangpo Grand Canyon pose high risk to the infrastructure in the region. In particular, the Zelunglung glaciers at the entrance of the canyon are experiencing rapid movements in the warming climate. This study presents a comprehensive assessment of glacier detachment risks based on remote sensing and physically based numerical analysis. Long-term meteorological records and debris-ice rheological modeling are used to reveal the volume and thickness of the instable source mass. An erosion–deposition debris flow analysis simulation program is employed to analyze multi-scenario hazard dynamic processes to predict the run-out distance, velocity, and deposition distributions. The deposition distributions along the river course in different glacier detachment scenarios are quantified to assess the size of possible barrier dam, which lays a good foundation for a quantitative risk assessment.

Keywords: Glacier landside; Climate change; Landslide dam; Risk assessment; Zelunglung Glacier; Yarlung Tsangpo Grand Canyon

INTRODUCTION

The Himalayan belt with extensive glaciered extent is sensitive to the changing climatic conditions and suffers from increasing glacier instabilities. Meanwhile, human activities in the mountain cryosphere, especially hydropower developments in Asian Water Tower, raise concerns about large-scale glacier detachments, which involve the release of massive sediments (volume>10^6 m^3) and the formation of barrier dams that block major river courses. The overtopping failures of these dams generates huge breaching floods that threat the downstream areas and induce upstream river-bank failures and inundation hazards. In particular, the large-scale hydropower project recently launched in the Yarlung Tsangpo Grand Canyon (YTGC), where several fast-moving valley glaciers are distributed, attract wide attention. For instances, the Chayu (Medog) earthquake (Mw 8.6) in 1950 triggered massive glacier detachments in the Zelunglung catchment in the YTGC and dammed the Yarlung Tsangpo (Kääb et al., 2021). The Sedongpu glacier detachment blocked the river on 17 October 2018, and the rapid rise in water level eventually caused dam overtopping, releasing a debris flood with a peak discharge of 32,000 m^3/s on 19 October (Chen et al., 2020).

In this region, numerous fast-moving mountain valley glaciers are distributed along the river channel, so that the YTGC is exposed to high risks of glacier hazards. These potential glaciers will threaten the construction and operational safety of the hydropower stations in this region (P1-P3 in Figure 1). Especially, the valley sediments in the Zelunglung catchment poses imminent threats. The potential glacier detachments that may occur in the future in the YTGC have not been systematically identified. The possible detached mass volume and barrier dam scale at different potential hazard spots remain clueless due to the lack of investigation.

Taking Zelunglung glacier as an example, this study presents a framework to quantify likely barrier dams caused by glacier detachments. Field investigations, remote sensing, and topographic analysis are conducted to forecast possible damming along the river course. Multi-scenario physically-based simulations are conducted to reveal the consequences of glacier detachments and river damming, and to investigate key influence factors.

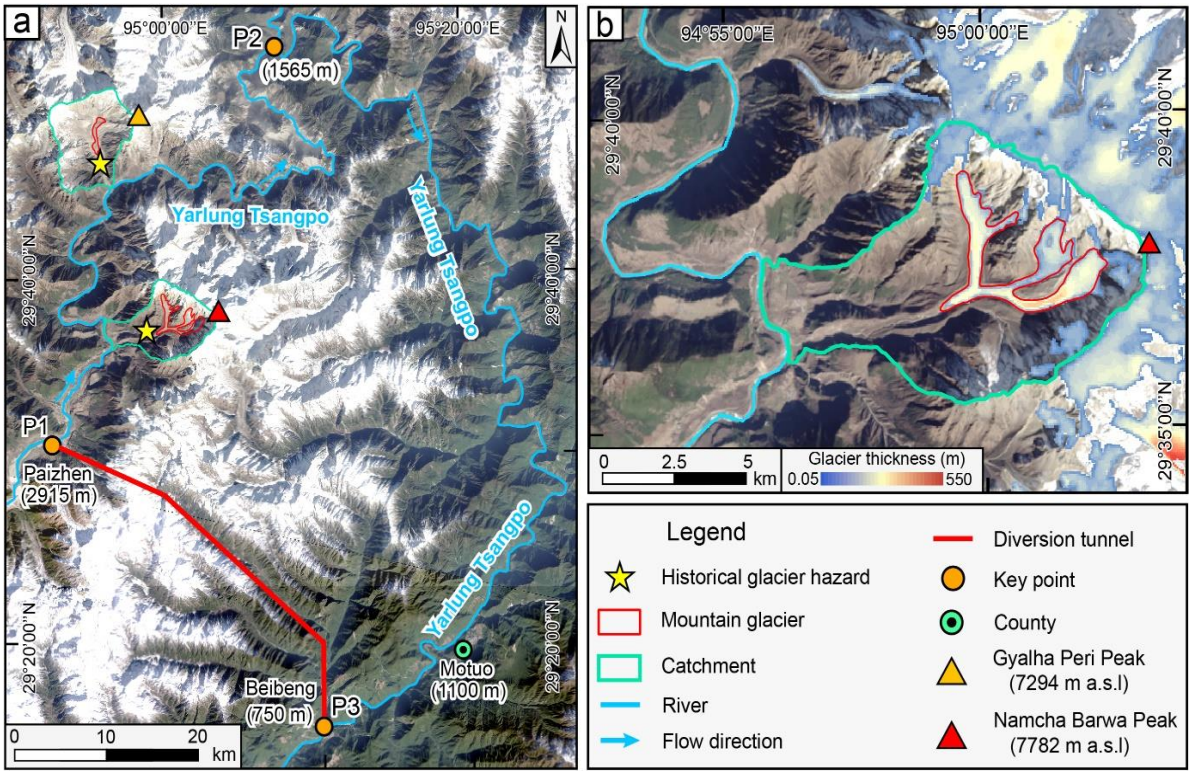

Figure 1. Research area in the Yarlung Tsangpo Grand Canyon. (a) Historical glacier detachments in the Sedongpu and Zelubnglung catchments, and a planned underground diversion tunnel for hydropower development; (b) Sediment thickness in the valley floor of the Zelunglung catchment.

RESEARCH AREA

As shown in Figure 1, the Zelunglung catchment is located on the right bank of the Yarlung Tsangpo Grand Canyon and the west slope of Namcha Barawa Peak (7782m a.s.l.). The catchment covers 53.62 km^2 with its elevations ranging from 2800 to 7782 m a.s.l. (Peng et al., 2022). Frequent glacier-related geohazards occurred at the upfront of the Zelunglung glacier including five massive glacier mass flows in 1950, 1968, 1973, 1984, and 2020 (Hu et al., 2020; Peng et al., 2022). Nearly 60 years of meteorological observations indicate a warming trend of

about 0.25-0.35℃/10 years. The average thickness and volume of sediments in the valley floor are approximately 200 m and 6.8×10^8 m^3, respectively (red curves in Figure 1b), which is calculated using the glacier flow model based on a shallow-ice approximation (Millan et al., 2022).

FIELD INVESTIGATION

The topographical characteristics, hydrological conditions, and geo-material properties were evaluated and determined through field investigations (Figure 2). An unmanned aerial vehicle (UAV), DJI Phantom 4 Pro RTK, was applied to obtain the overview of the eroded gully bed. The geometry and deposit deposition at the outlet of the catchment were measured using UAV and a laser range finder. In-situ geo-material samples were collected near the Zhibai Bridge at the outlet of the Zelunglung catchment and typical particle size distributions were obtained based on sieving tests. Sand cone tests using China ISO standard sand were conducted to determine the density of geo-materials and soil particle. The other physical properties of in-situ samples for a physically-based simulation model were determined as shown in next section.

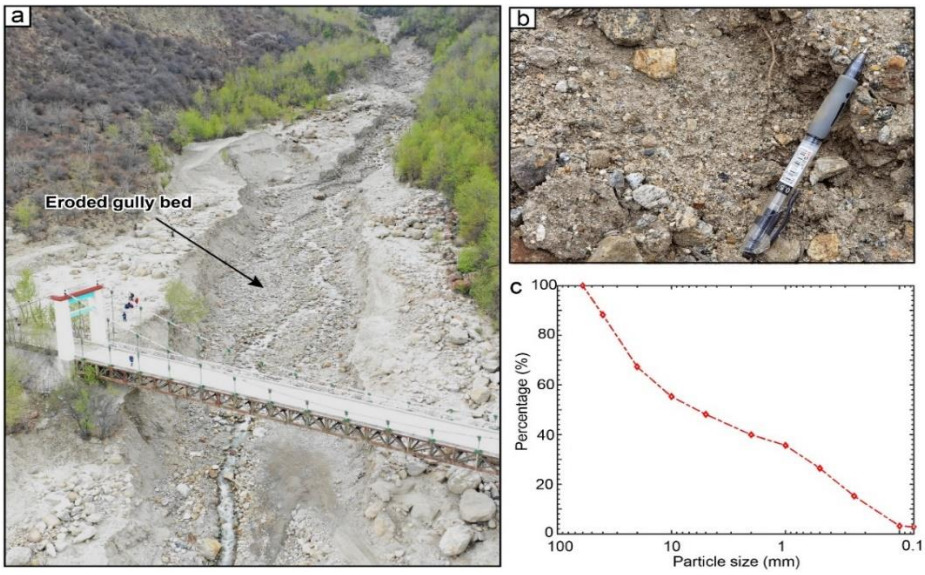

Figure 2. Field investigations at the Zelunglung catchment. (a) Outlet of catchment and eroded gully bed. (b) In-situ sediment samples. (c) Particle size distribution of the samples.

SIMULATION FRAMEWORK

The multi-scenario cell-based analysis of the mass flows is conducted using an Erosion–Deposition Debris Flow Analysis program (EDDA) (Chen and Zhang, 2015; Shen et al., 2020). The deposit thickness of the flow mass caused by detachments of valley sediments is quantified using EDDA. The governing equations of mass flow dynamics are shown below:

$$\frac{\partial h}{\partial t}+\frac{\partial (hv_x)}{\partial x}+\frac{\partial (hv_y)}{\partial y}=i\left[C_{v*}+(1-C_{v*})s_b\right]+A\left[C_{vA}+(1-C_{vA})s_A\right] \quad (1)$$

$$\frac{\partial(C_v h)}{\partial t}+\frac{\partial(C_v h v_x)}{\partial x}+\frac{\partial(C_v h v_y)}{\partial y}=iC_{v*}+AC_{vA} \tag{2}$$

$$\frac{\partial v_x}{\partial t}+v_x\frac{\partial v_x}{\partial x}=g\left[-\mathrm{sgn}(v_x)S_{fx}-\frac{\partial(z_b+h)}{\partial x}\right] -v_x\frac{i\left[C_{v*}+(1-C_{v*})s_b\right]+A\left[C_{vA}+(1-C_{vA})s_A\right]}{h} \tag{3}$$

$$\frac{\partial v_y}{\partial t}+v_y\frac{\partial v_y}{\partial y}=g\left[-\mathrm{sgn}(v_y)S_{fy}-\frac{\partial(z_b+h)}{\partial y}\right] -v_y\frac{i\left[C_{v*}+(1-C_{v*})s_b\right]+A\left[C_{vA}+(1-C_{vA})s_A\right]}{h} \tag{4}$$

where the flow velocities along the *x*- and *y*-directions are represented as v_x and v_y, respectively; *t* and *h* are time and the flow depth, respectively; $i=\partial z_b/\partial t$ is the erosion or deposition rate; z_b is the channel bed elevation; *A* represents the entrainment rate; g=9.81m/s^2 is the gravitational acceleration; C_V is the volumetric sediment concentration of the mass flow; C_{VA} and C_{V*} are the volume fractions of solids in the entrained materials and erodible channel bed, respectively; s_A and s_b are the saturation degrees in the entrained materials and the erodible bed, respectively; The $sgn(\cdot)$ represents a *sgn* function satisfying $sgn(x)=1(x>0)$, $sgn(x)=0(x=0)$ and $sgn(x)=-1(x<0)$, reflecting that the direction of resistance is opposite to the flow direction; S_{fx} and S_{fy} indicate the flow resistance slopes in the *x*- and *y*-directions, which are calculated using the model developed by Julien and Lan (1991) when $C_V > 0.2$:

$$S_f=\frac{\tau_y}{\rho g h}+\frac{K\mu V}{8\rho g h^2}+\frac{n_{td}^2V^2}{h^{4/3}} \tag{5}$$

where τ_y is the yield stress of the debris flow; ρ is the mass density of the mixture; μ and *K* indicate the dynamic viscosity and the laminar flow resistance, respectively; n_{td} is an equivalent Manning coefficient of the flowing mixture:

$$n_{td}=0.0538ne^{6.0896C_V} \tag{6}$$

where *n* indicates the Manning coefficient. τ_y and μ are calculated using empirical relationships developed by O'Brien and Julien (1988):

$$\tau_y=\alpha_1 e^{\beta_1 C_V} \tag{7}$$

$$\mu=\alpha_2 e^{\beta_2 C_V} \tag{8}$$

where α_1, α_2, β_1 and β_2 are empirical parameters. When C_V is smaller than 0.1, τ_y is calculated as:

$$\tau_y = (1-C_s)C_V(\rho_s - \rho_w)gh\cos\theta^2\tan\phi \tag{9}$$

where C_s represents the coefficient of suspension of solid particles and $(1 - C_s)$ is the solid portion that is in contact with erodible channel bed; θ is the slope angle; ρ_s and ρ_w are the density of solids and water, respectively; ϕ is the friction angle of the solid particles contacting the bed.

Bed erosion occurs in the motion of the flowing mixture when the bed shear stress is larger than the critical erosive shear stress and C_V is smaller than an equilibrium value $C_{v\infty}$ (Takahashi et al., 1992):

$$C_{v\infty} = \frac{\rho_w \tan\theta}{(\rho_s - \rho_w)(\tan\phi_{bed} - \tan\theta)} \tag{10}$$

where ϕ_{bed} is the internal friction angle of the erodible basal bed. The erosion rate is quantified using the model from Hanson and Simon (2001) as:

$$i = K_e(\tau - \tau_c) \tag{11}$$

where K_e is an erosion coefficient; τ_c is the critical erosive shear stress, and τ_c is he critical erosive shear stress. We calculate these two parameters based on the following equations according to Chang et al (2010; 2011):

$$K_e = 20075e^{4.77}C_u^{-0.76} \tag{12}$$

$$\tau_c = \frac{2}{3}gd_{50}(\rho_s - \rho_w)\tan\phi \tag{13}$$

where e is the void ratio; C_u=d_{50}/d_{10} is the coefficient of uniformity, in which d_{10} and d_{50} are particles sizes 10% and 50% finer; respectively; ρ_s and ρ_w are the mass density of soil particle and water, respectively; ϕ is the friction angle. For the Zelunglung Glacier, we take the same erosion rate reported in Peng et al., (2022). The shear stress can be calculated as Graf (1984):

$$\tau=\rho ghS_f \tag{14}$$

The deposition process of solid material occurs if $C_V > C_{v\infty}$. The deposition rate i can be quantified as (Takahashi et al., 1992):

$$i = C_{dep}(1-\frac{V}{pV_e})\frac{C_{v\infty} - C_v}{C_{v*}}V \tag{15}$$

$$V_e = \frac{2}{5d_{50}}\left(\frac{g\sin\theta_e\rho}{0.02\rho_s}\right)\lambda^{-1}h^{1.5} \quad (16)$$

where C_{dep} is a deposition rate coefficient; V and V_e are the flow velocity and critical flow velocity, respectively; d_{50} and ρ are the median diameter of particles and the density of the mixture, respectively. The values of all inputs of EDDA simulation model are summarized in Table 1.

Table 1. Simulation parameters

$\rho_s(kgm^{-1})$	d_{50} (mm)	$C_v{}^*$	$C_v channel$	$C_v sediment$	C_s	$\tau_c\ (Pa)$	$K_e\ (m^3Ns^{-1})$	C_{dep}
2700	10	0.7	0.5	0.65	0.6	50	1.5×10^{-7}	0.03

Note: $C_V channel$ and $C_V sediment$ are the volumetric ratio of solid of deposits along valley channel and detached glacier valley geo-materials, respectively.

HAZARD SCENARIO SETTING AND MODEL SET-UP

Model setup. Given that the length of valley debris glacier is much larger than its width, the detached length of valley debris glacier is taken to quantify the multi-scenario glacier detachments. Figure 3a reveals that detached lengths of world-wide historical detachments are in the range of 0.4 – 3.6 km with a median of 1 km and an average of 1.5 km (data sources: Schneider et al., 2011; Petrakov et al., 2008). Therefore, we consider four scenarios for the Zelunglung glacier, including 1-km, 2-km and 3-km detached lengths, and the detachment of all sediments. Figure 3b shows the set-up of EDDA simulation model where green, orange and red curves represent the EDDA calculation range, eroded channel material and valley glacier sediment, respectively. L_g represents the detached length of valley glacier, and the released source geo-materials are different for different L_g values in the multi-scenario analysis, which can produce different sizes of barrier dams along the river course.

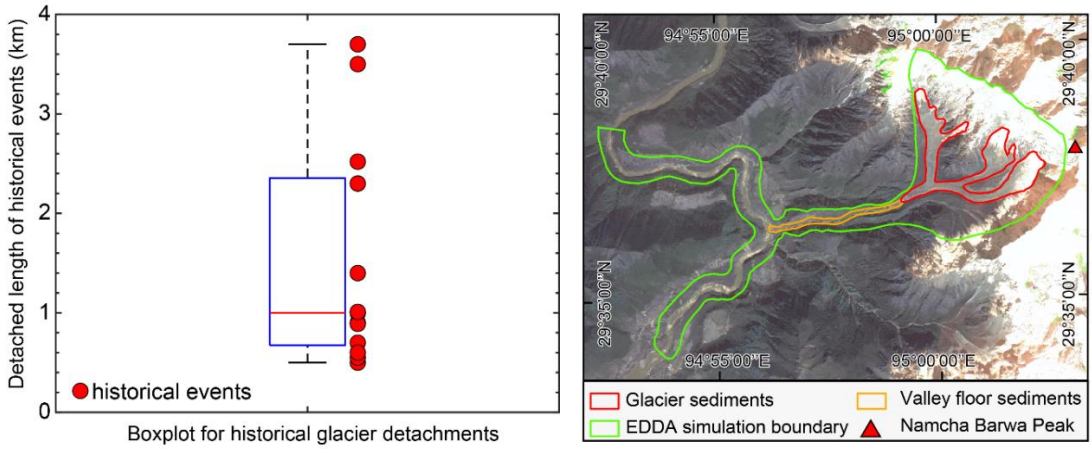

Figure 3. Detached lengths of world-wide historical glacier detachments in the Zelunglung catchment and model set-up. (a) Detached length of historical debris-ice glacier. (b) Simulation boundaries of the EDDA model for Zelunglung Glacier.

Simulation results. Figure 4 shows typical flow dynamic process of the mass flow caused by glacial sediment detachments. The front velocity of the mass flow is about 30 m/s when sediment detached from a relatively steep slope (Figure 4a). The moving velocity is reduced to about 20 m/s when flowing onto the valley floor with a gentle slope, and then the detached mass maintains this flowing velocity until rushes into the river course (Figures 4b and c). The geo-material flowing into the river continues to move along the river course (15 m/s), and finally forms a barrier dam. The entrainment volumes in the multi-scenario simulations are less than 100 million m^3. The key reason for the relatively low velocity of mass flows is the gentle slope of the valley channel.

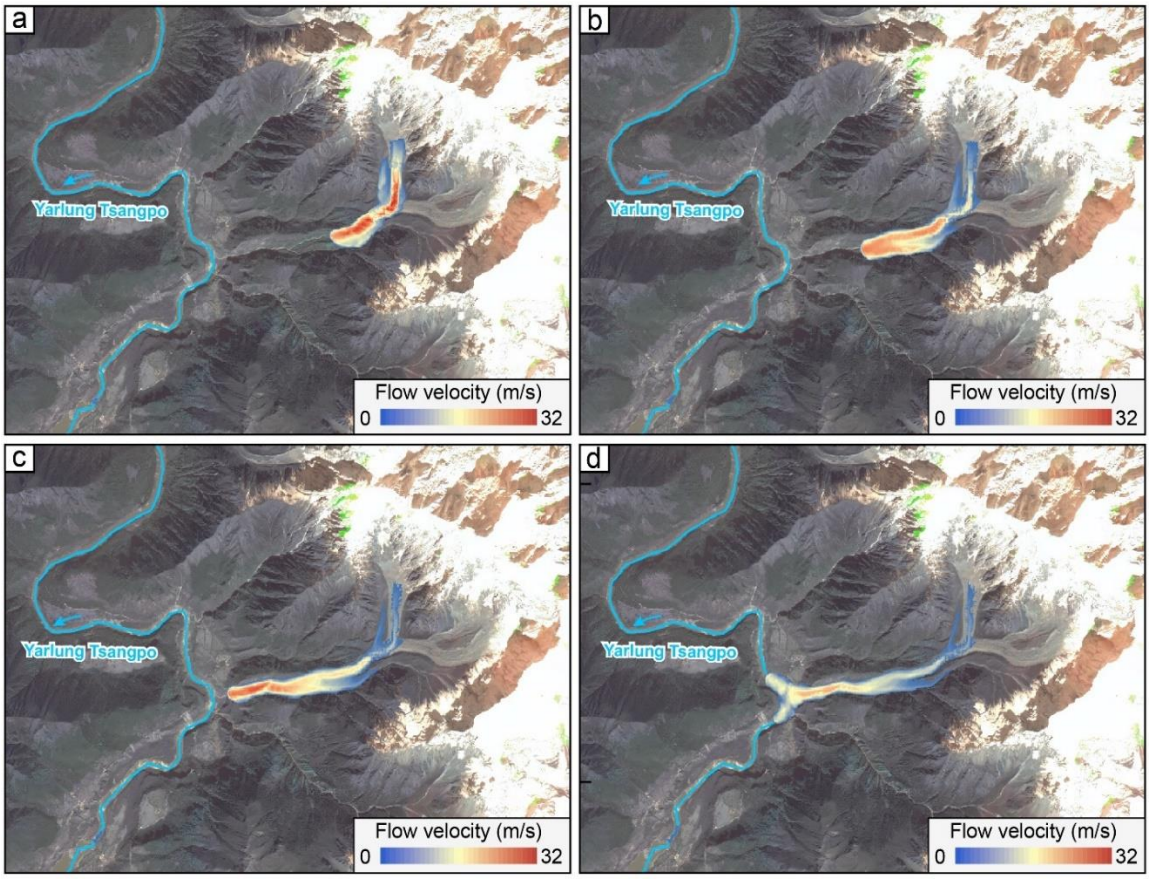

Figure 4. Simulated flow velocity of mass flow for Lg = 3 km. (a) *t* = 60 s; (b) *t* = 120 s; (c) *t* = 180 s; (d) *t* = 240 s.

Figure 5 shows simulated deposition thickness along the river course. There is almost no river deposit and has no impact on the river flow when a relatively small-scale detachment happens (L_g = 1 km). Most of the detached mass remains in the valley floor (Figure 5a). The average height of the formed barrier dams is less than 30 m when L_g = 2 km. By contrast, a massive detachment of Lg≥3 km causes large-scale river damming. If the detached length is 3 km, the same as the 2018 Sedognpu hazard in this region, the barrier dam is more than 60 m high and 5 km long (Figure 5c). Although the instability of all glacier sediment is very unlikely (Figure 3a), the consequences are more serious. The length of the affected river reaching more than 10 km and the height of the barrier dam will exceed 100 m (Figure 5d).

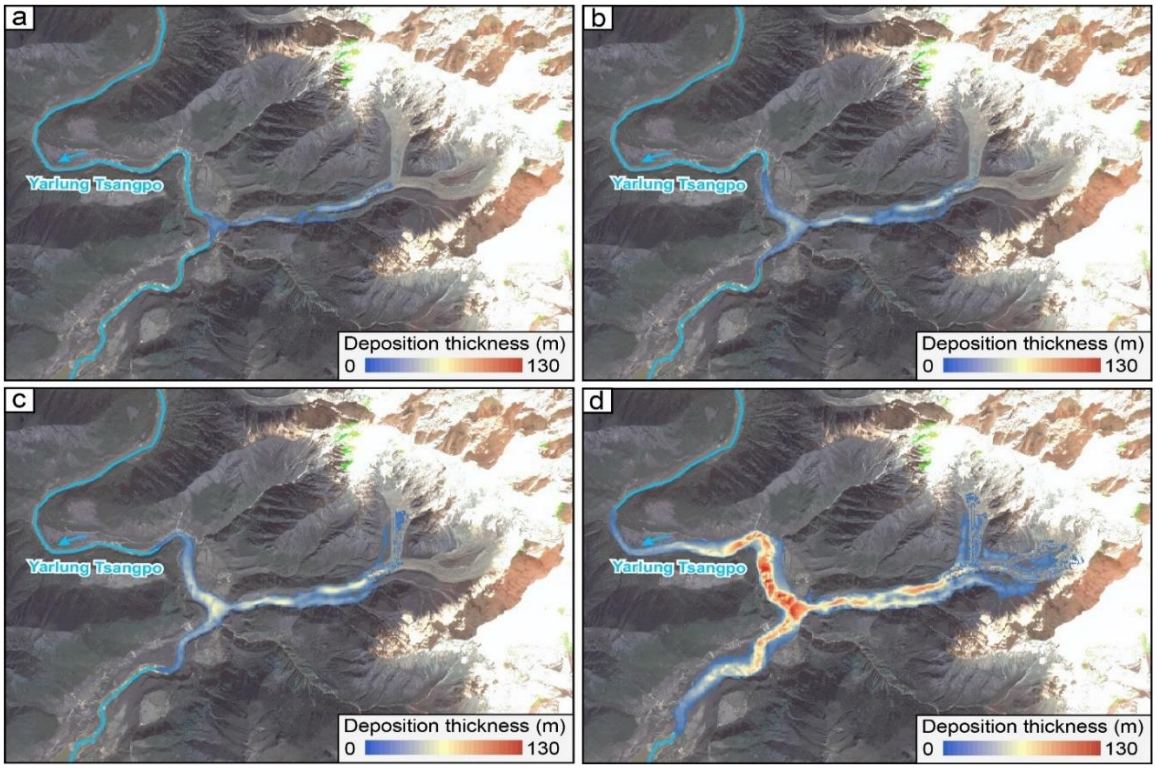

Figure 5. Multi-scenario EDDA simulation results of river deposits. (a) L_g = 1 km; (b) L_g = 2 km; (c) L_g = 3 km; (d) Detachment of all valley sediment.

SUMMARY

Fast-moving valley glaciers raise concerns about their potential threats of river damming and damage to mega-hydropower projects in the Asian Water Tower, especially in the wake of two detachments in 2018 in the Yarlung Tsangpo Grand Canyon. Taking the Zelunglung glacier as an example, this study delivers a quantitative framework to evaluate damming threats caused by detachments of massive valley debris glaciers based on in-situ investigations, remote sensing and physically-based simulation program. The results reveal that the average thickness of valley sediments in the Zelunglung catchment is 200 m and the total sediment volume is more than 680 million m^3. Relatively small-scale sediment detachment (i.e Lg=1 km) has limited impacts on the river course, and the average height of the formed barrier dams are less than 30 m. By contrast, a massive detachment (Lg>3 km) can cause large-scale river damming as that in the 2018 Sedognpu hazard in this region. The analysis outcome provides a clue to investigate consequences caused by glacier detachments, and helps analyze potential barrier dams and their impacts on the hydropower developments in the Himalayan region.

ACKNOWLEDGMENTS

This work is supported by the National Natural Science Foundation of China (No. U20A20112), the Research Grants Council of the Hong Kong SAR (Grant Nos. N_HKUST620/20 and 16209421) and Hetao Shenzhen-Hong Kong Science and Technology Innovation Cooperation Zone (Project No. HZQB-KCZYB-2020083).

REFERENCES

Chang, D. S., and Zhang, L. M. (2010). "Simulation of the erosion process of landslide dams due to overtopping considering variations in soil erodibility along depth." *Nat. Hazard. Earth. Sys.*, 10, 933–946.

Chang, D. S., Zhang, L. M., Xu, Y., and Huang, R. Q. (2011). "Field testing of erodibility of two landslide dams triggered by the 12 May Wenchuan earthquake." *Landslides* 8, 321–332.

Chen, C., Zhang, L. M., Xiao, T., and He, J. (2020). "Barrier lake bursting and flood routing in the Yarlung Tsangpo Grand Canyon in October 2018." *J. Hydrol.*, 583, 124603.

Chen, H. X., and Zhang, L. M. (2015). "EDDA 1.0: integrated simulation of debris flow erosion, deposition and property changes." *Geosci. Model. Dev.*, 8, 829–844.

Graf, W. H. (1984). *Hydraulics of sediment transport*, Water Resources Publications, Colorado.

Hanson, G. J., and Simon, A. (2001). "Erodibility of cohesive streambeds in the loess area of the midwestern USA." *Hydrol. Process.*, 15(1), 23–38.

Hu, K. H., Zhang, X. P., You, Y., Hu, X. D., Liu, W. M., and Liu, Y. (2019). "Landslides and dammed lakes triggered by the 2017 Ms6.9 Milin earthquake in the Tsangpo Gorge." *Landslides*, 16, 993–1001.

Julien, P. Y., and Lan, Y. (1991). "Rheology of hyper concentrations." *J. Hydraul. Res.*, 117(3), 346–353.

Kääb, A., Jacquemart, M., Gilbert, A., Leiness, S., Girod, L., and Huggel, C. (2021). "Sudden large-volume detachments of low-angle mountain glaciers - more frequent than thought?" *The Cryosphere*, 15, 1751–1785.

Millan, R., Mouginot, J., Rabatel, A., and Morlighem, M. (2022). "Ice velocity and thickness of the world's glaciers." *Nat. Geosci.*, 15, 124–129.

O'Brien, J. S., and Julien, P. Y. (1988). "Laboratory analysis of mudflow properties." *J. Hydraul. Res.*, 114, 877–887.

Peng, D. L., Zhang, L. M., Jiang, R. C., Zhang, S., Shen, P., Lu, W. J., and He, X. (2022). "Initiation mechanisms and dynamics of a debris flow originated from debris-ice mixture slope failure in southeast Tibet, China", *Eng. Geol.*, 307, 106783.

Petrakov, D. A., Chernomorets, S. S., Evans, S. G., and Tutubalina, O. V. (2008). "Catastrophic glacial multi-phase mass movements: a special type of glacial hazard." *Adv. Geosci.*, 14, 211–218.

Schneider, D., Huggel, C., Haeberli, W., and Kaitna, R. (2011). Unraveling driving factors for large rock-ice avalanche mobility, *Earth. Surf. Proc. Land.*, 36, 198–1966.

Shen, P., Zhang, L., and Wong, H. F. (2020). "Debris flow enlargement from entrainment: A case study for comparison of three entrainment models." *Eng. Geol.*, 270, 105581.

Takahashi, T., Nakagawa, H., Harada, T., and Yamashiki, Y. (1992). "Routing debris flows with particle segregation." *J Hydraul Eng*, 118(11), pp: 1490–1507.